

Photon Counting Interferometry to Detect Geotropic Space-Time Fluctuations with GQuEST

Sander M. Vermeulen,^{1,*} Torrey Cullen,¹ Daniel Grass,¹ Ian A. O. MacMillan,¹ Alexander J. Ramirez,¹ Jeffrey Wack,¹ Boris Korzh,² Vincent S. H. Lee,¹ Kathryn M. Zurek,¹ Chris Stoughton,³ and Lee McCuller¹

¹*Division of Physics, Mathematics and Astronomy,
California Institute of Technology, Pasadena, CA 91125*

²*NASA Jet Propulsion Laboratory, Pasadena, CA 91109*

³*Fermi National Accelerator Laboratory, Batavia, IL 60510*

(Dated: April 12, 2024)

The GQuEST (Gravity from the Quantum Entanglement of Space-Time) experiment uses tabletop-scale Michelson laser interferometers to probe for fluctuations in space-time. We present an interferometer design featuring a novel photon counting readout method that provides unprecedented sensitivity, as it is not subject to the interferometric standard quantum limit. We evaluate the potential of this design to measure space-time fluctuations motivated by recent ‘geotropic’ quantum gravity models. The accelerated accrual of statistical power offered by the photon counting readout enables GQuEST to detect the predicted quantum gravity phenomena within measurement times at least 100 times shorter than equivalent conventional interferometers. The GQuEST design thus enables a fast and sensitive search for signatures of quantum gravity in a laboratory-scale experiment.

1. INTRODUCTION

The aim of the study of quantum gravity is to find a description of gravitation in concordance with quantum mechanics. Quantum gravity research is challenged by the vast difference in the scale of theoretically predicted gravity phenomena and the scale of quantum phenomena that can be measured in experiments. However, a number of different theories propose that the quantum nature of gravity implies fluctuations of the space-time metric that accumulate over macroscopic distances and yield potentially measurable uncertainties [1–5].

We focus here on ‘geotropic’ fluctuations as proposed by Verlinde & Zurek [4]; this theory provides a concrete prediction for a quantum gravity signal expected in interferometers. These fluctuations of space-time geometry are associated with quantum degrees of freedom counted by entanglement entropy.

When a photon propagates in a metric that exhibits these fluctuations, it accumulates a change of phase compared to the case without fluctuations. When one compares the phase of two photons propagating along different paths in this randomly fluctuating metric, as in a Michelson interferometer, the observed phase difference will vary in a way characteristic of the space-time fluctuations.

In Section 2.a, we discuss the theoretical motivation for these fluctuations in the metric from quantum gravity. In Section 2.b we describe how a signal from geotropic space-time fluctuations appears in interferometers. In Section 3 we present our experimental approach of using a Michelson interferometer with a novel ‘photon counting’ readout method to detect this signal and compare the detection statistics of this new approach with those of the standard

‘homodyne readout’ scheme. We present our interferometer design, optimized for counting, and projected reference sensitivity in Section 4. Section 5 discusses our strategy of a staged construction of the experiment, which is designed to positively identify a quantum gravity signal and distinguish it from known effects. We conclude in Section 6. A detailed consideration of the experimental challenges and sources of noise is included in the Appendix.

2. THEORETICAL MOTIVATION

2.a. Quantum Gravity Model

The status of theoretical results building on the work of Verlinde & Zurek et al. (VZ) up to the year 2022 is summarized in [6], showing that diverse theoretical approaches predict metric fluctuations of the same scale. The pixellon model was proposed in Ref. [7] to give detailed predictions for interferometric measurements based on the general theoretical expectations proposed by VZ. Refs. [8, 9] describe how shock-wave geometries give rise to these fluctuations. Details of the sensitivity of interferometers to geotropic fluctuations modeled by the pixellon are described in Ref. [10] with several testable predictions for the power spectral density, angular correlations, and low-frequency (IR) cut-off of the signal. It was also found in Ref. [11] that geotropic fluctuations would severely impact the sensitivity of future gravitational wave detectors.

The quantum gravity theory behind VZ geotropic fluctuations incorporates the entanglement of quantum states on surfaces that define regions of space (see e.g. Refs. [12–14]). These states are not directly observable. However, an essential conclusion of the theory is accessible to experimental tests: the presence of an isotropic, spherical breathing perturbation of the metric, which can be de-

* smv@caltech.edu

scribed by the pixellon scalar field ϕ [7, 10],

$$ds^2 = -dt^2 + (1 - \phi)(dr^2 + r^2 d\Omega^2). \quad (1)$$

The theory by VZ proposes degrees of freedom that fluctuate from entanglement entropy, and this scalar field represents the influence of those degrees on gravitation. This field ϕ is predicted to obey a wave equation and have a thermal distribution with Bose-Einstein statistics [7]. The GQuEST experiment will measure or constrain the metric fluctuations from the scalar field ϕ .

Theories of geotropic fluctuations consistently determine that the scale of RMS length fluctuations accumulated over a distance L is given by

$$\langle \delta L^2 \rangle = \alpha \frac{l_p L}{4\pi} \approx \alpha (5.7 \cdot 10^{-18} \text{ m})^2 \left(\frac{L}{5 \text{ m}} \right), \quad (2)$$

where we use a convention for the Planck length of $l_p = \sqrt{8\pi\hbar G/c^3} = 8.1 \cdot 10^{-35} \text{ m}$, and L is the measurement length. For reference, we normalize L to an experimental scale of 5 m. Theoretical uncertainty in the fluctuation magnitude is encapsulated in the parameter α (note $\langle \phi^2 \rangle \propto \alpha$). Of particular note is that diverse approaches to quantum gravity yield $\alpha = \mathcal{O}(1)$. These include analyses from conformal field theory [14], dilaton theory [15], and hydrodynamics [16]. We expect that with further development of the theoretical tools, α will be calculated exactly.

We take $\mathcal{O}(x)$ to denote an order-of-magnitude estimate of x , specifically $\mathcal{O}(x) = y \Rightarrow 10^{-0.5}y < x < 10^{+0.5}y$. Our use of the approximation symbol, \approx , indicates accuracy to the number of expressed significant digits.

2.b. Interferometer Signal from Geotropic Fluctuations

A laser interferometer (IFO) uses laser light to measure the accumulated phase difference between light traversing two arms. The accumulated phase differences in an interferometer due to the geotropic fluctuations are stochastic and must be described statistically. We use the power spectral density (PSD) of the phase differences that geotropic fluctuations impart on the light to motivate, design, and benchmark experimental tests. We express the PSD in terms of the effective optical path length differences δL corresponding to the measured phase fluctuations in an interferometer $S_L^\phi(f)$ (which is normalized as a single-sided PSD, as a function of frequency $0 < f < \infty$). This PSD is the Fourier transform of the auto-correlation function of the length changes corresponding to accumulated phase differences of light returning to the beamsplitter (according to the Wiener-Khinchin theorem).

The PSD is computed in Ref. [10] using the pixellon model [7]. This model is a low-energy effective description of the complete theory. The pixellon model PSD is depicted in Fig. 1. Note, however, that a *derivation* of the pixellon model from a full theory (i.e. one that also works at high energy, that is UV-complete) is still underway. Several specific properties of this theoretical PSD are relevant for

calculating experimental requirements. The peak level of the spectral density, $\overline{S}_L^\phi \equiv S_L^\phi(f_{\text{pk}}) \geq S_L^\phi(f)$ is given by [10]:

$$\overline{S}_L^\phi = \alpha \frac{l_p L^2}{8\pi^2 c} \approx \alpha \left(2.9 \cdot 10^{-22} \frac{\text{m}}{\sqrt{\text{Hz}}} \right)^2 \left(\frac{L}{5 \text{ m}} \right)^2. \quad (3)$$

The signal power scales with the measurement length as L^2 . It also scales with the free theoretical parameter α , which we seek to measure or bound. Current theoretical expectation, based on [4, 14, 15, 17], corresponds to $\alpha \lesssim 1$. Note that we denote the peak value or most representative level of the signal and other spectra with an over-bar (\overline{S}) from here on.

The peak of the spectrum is at $f_{\text{pk}}(L) = \mathcal{O}(c/[2\pi L])$, with a signal bandwidth $\Delta f(L) = \mathcal{O}(c/[2\pi L])$. From numerical evaluations of the PSD, we compute the specific values

$$f_{\text{pk}} \approx 15.6 \text{ MHz} \left(\frac{5 \text{ m}}{L} \right), \quad \Delta f \approx 36 \text{ MHz} \left(\frac{5 \text{ m}}{L} \right), \quad (4)$$

As is clear from Fig. 1, the signal is broadband with multiple peaks, and the definition of the signal bandwidth is somewhat arbitrary. The 3-dB full-width-half-maximum bandwidth, which is approximately 16 MHz, is not suitable here; instead, we use $\Delta f \approx 36 \text{ MHz}$ as motivated from detection statistics in the following section.

We note that the signal amplitude depends on the angle between the two IFO arms Θ . The signal amplitudes indicated in this work are for $\Theta = 90^\circ$. The amplitude decreases to zero as $\Theta \rightarrow 0^\circ$. The precise angular correlation is discussed in [4, 10].

The use of two instruments to detect geotropic fluctuations can be advantageous, as the signal is expected to be correlated for co-located IFOs, and dominant noises are not. Two co-located IFOs have a signal coherence characterized by the separation between their beamsplitters, L_{sep} . Following the treatment in [11] the coherence at f_{pk} is 0.88 for $L_{\text{sep}}/L = 0.3$.

2.c. Limits from Existing Experiments

Quantum space-time fluctuations have not yet been observed. However, existing interferometric experiments and astronomical observations impose tentative constraints on the phenomenology.

The LIGO interferometers are the most sensitive in terms of detectable strain fluctuations in their sensitive bandwidth [18]. However, these 4-km instruments have reduced sensitivity at their respective peak geotropic signal frequency (i.e. at $f_{\text{pk}}(4 \text{ km}) \approx 20 \text{ kHz}$). The Fermilab Holometer comprised a pair of co-located 40-m IFOs and was built to be sensitive at frequencies on the order of $f_{\text{pk}}(40 \text{ m}) \approx 2 \text{ MHz}$ [19]. The strongest experimental constraints on the strength of the fluctuations α therefore come from LIGO and Holometer measurements, which at 3σ significance, are roughly $\alpha \lesssim 3$ and $\alpha \lesssim 0.7$ (with IR cut-off), and $\alpha \lesssim 0.1$ and $\alpha \lesssim 0.6$ (without IR cut-off), respectively [10].

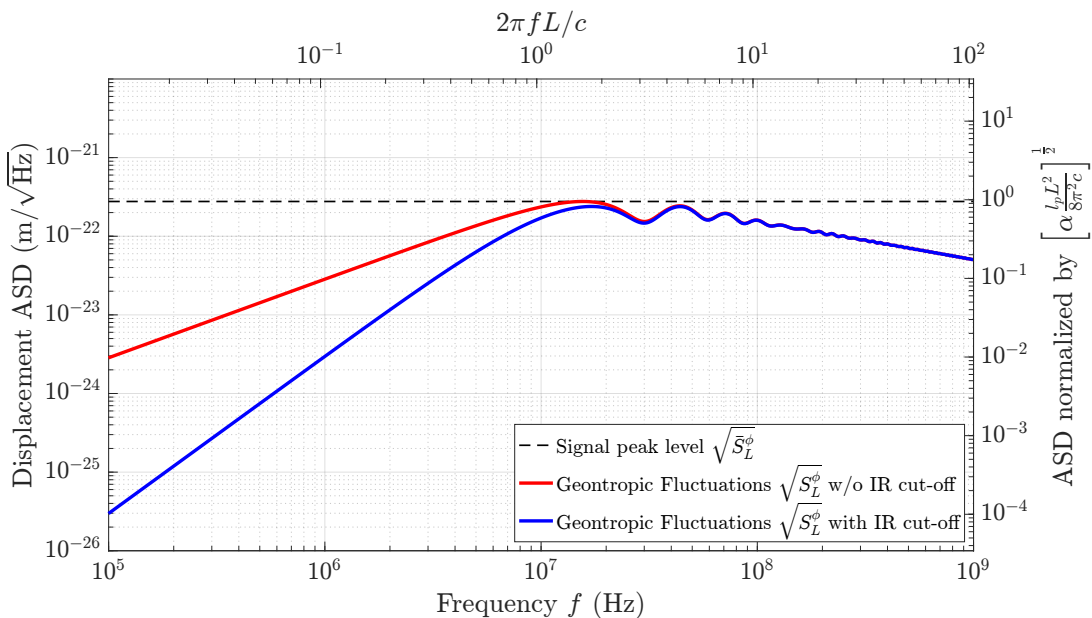


FIG. 1. The predicted displacement amplitude spectral density (ASD) signal due to geotropic fluctuations in the GQuEST experiment, assuming an arm length $L = 5$ m and $\alpha = 1$. The ASD is based on the ‘pixellon’ model of geotropic fluctuations [10], and two different variations are shown, one where the signal spectrum has a low-frequency or IR cut-off at a frequency c/L , and one without this IR cut-off. The top x-axis shows the angular signal frequency $2\pi f$ normalized by the light-crossing frequency c/L . The y-axis on the right shows the signal ASD normalized to the fundamental scale $\alpha l_p L^2 / (8\pi^2 c)$, as used in [10].

An experiment similar to GQuEST, called QUEST [20], is currently being commissioned at Cardiff University. QUEST comprises a pair of co-located table-top IFOs using homodyne readout and is designed to exceed the sensitivity of the Holometer by using higher optical powers and by using squeezed states of light. At its proposed sensitivity, QUEST could probe values of $\alpha < 0.6$ (with or without IR cut-off) with 3σ significance in roughly five months of observation time.

Space-time fluctuations could potentially manifest in experimental observations other than interferometric measurements. For instance, images of distant astronomical objects should appear blurred as the phase front of the light is distorted by space-time fluctuations. By analyzing data from astronomical observations, constraints were set on the strength of potential space-time fluctuations [21, 22] subject to important caveats [4, 23]. Importantly, the transverse correlations of geotropic fluctuations render these constraints inapplicable to the theory considered here [24].

3. EXPERIMENTAL APPROACH

3.a. Laser Interferometry

A laser Michelson interferometer (IFO) operates by shining laser light at a beamsplitter, which splits light into two arms delimited by end mirrors; the end mirrors reflect the light back which is then recombined at the beamsplitter where it interferes. Any signal that perturbs the opti-

cal path length of light traveling inside an interferometer causes a phase modulation of the light in the arm. This can equivalently be described as the conversion of input laser light to light with frequency components that are offset from the source frequency; the resulting frequency components of the optical field are typically called sidebands. For a signal perturbation (i.e. a modulation) at frequency f , the input laser field, also called the carrier field, at frequency $\nu = c/\lambda = ck$ (where λ , k are the laser wavelength and wavenumber, respectively) is modulated to create sideband fields at frequencies $\nu + f$ and $\nu - f$.

By introducing a static difference in the optical path lengths of the arms, constructive interference at one port of the beamsplitter is produced, which gives rise to ‘fringe’ light at the IFO’s output. Perturbations of the arm lengths then produce modulations of this light level, allowing the difference in arm length to be inferred by continuously monitoring the output light power P_{out} . Equivalently, the observed modulation of P_{out} can be described as due to the beating of sideband fields with the fringe light field. This readout technique for interferometric signals is called ‘DC readout’ or ‘fringe readout’ in the interferometry community, as it uses the constant-intensity or DC (fringe) light as a local oscillator. The use of a local oscillator field makes this a form of optical homodyne readout, analogous to homodyne detection in radio and microwave electronic systems.

The following sections calculate the quantum limits to resolving geotropic signals with an interferometer, first by using the DC (or ‘fringe’) readout method, henceforth referred to more generally as homodyne readout, and second

by directly detecting the power in optical sidebands.

3.b. Homodyne Readout

The local oscillator field light power P_{out} randomly varies due to photon shot noise [25, 26], limiting the ability to resolve small modulations of P_{out} due to signals. When operating the IFO at near-perfect destructive interference, the shot noise level, expressed as a one-sided spectral density of the equivalent differential arm length perturbations, does not depend on the choice of local oscillator power P_{out} , only on the circulating power on the beamsplitter, P_{BS} . The standard quantum limit from shot noise (SQL) is [27, 28]:

$$\bar{S}_L^q = \frac{\hbar c}{2kP_{\text{BS}}} \approx \left(6.2 \cdot 10^{-19} \frac{\text{m}}{\sqrt{\text{Hz}}}\right)^2 \left(\frac{10 \text{ kW}}{P_{\text{BS}}}\right) \left(\frac{\lambda}{1550 \text{ nm}}\right). \quad (5)$$

The interferometric SQL can equivalently be described as arising due to the interaction of the circulating light field with the vacuum (see below). It applies to any form of homodyne readout of an IFO. We express Eq. (5) using the optical wavelength and power at the beamsplitter from the reference design in Section 4.

This noise level \bar{S}_L^q is only one of many noise contributions; the other noises arise from classical processes that create fluctuations of the IFO arm length or the phase and amplitude of the light. At the signal peak frequency, these classical noises can be engineered to be substantially smaller than the quantum noise \bar{S}_L^q . However, the classical noises will not be negligible when photon counting, described in Section 3.c, is used.

The peak signal level \bar{S}_L^ϕ given by Eq. (3) is below the shot noise \bar{S}_L^q given by Eq. (5) by seven orders of magnitude. However, given sufficient measurement time, conventional interferometers using homodyne readout could eventually detect the signal. The geotropic fluctuations \bar{S}_L^ϕ manifest as a stochastic noise-like broadband displacement signal and this can be detected as excess noise on top of the known quantum shot noise. We define the signal-to-noise ratio (SNR) as the ratio of the mean level of the reference signal over the statistical standard error in its measurement via a maximum likelihood estimator. The SNR of an optimal estimator in a search for excess noise due to geotropic fluctuations in a shot-noise-limited interferometer using homodyne readout is given by [28–31]

$$\text{SNR}_{\text{homodyne}}^2 = \int_0^T \int_0^\infty \left(\frac{S_L^\phi(f)}{\bar{S}_L^q(f)}\right)^2 df dt \approx T \Delta f \left(\frac{\bar{S}_L^\phi}{\bar{S}_L^q}\right)^2 \quad (6)$$

$$\approx \alpha^2 \left(\frac{T}{6 \cdot 10^5 \text{ s}}\right) \left(\frac{P_{\text{BS}}}{10 \text{ kW}}\right)^2 \left(\frac{L}{5 \text{ m}}\right)^3, \quad (7)$$

where T is the integrated measurement time, and the time required to achieve a $\text{SNR}^2 = 1$ or 1σ significance test for $\alpha = 1$ would be around 160 hours of continuous

operation. A $\text{SNR}^2 = 9$ or 3σ significance test for $\alpha = 1$ would then be around two months of continuous operation. Note that our definition of Δf as stated above is chosen to make the approximation of Eq. (6) exact, to account for the specific spectral shape of the signal for homodyne readout searches.

This suggests that a 5-m IFO using homodyne readout is a feasible means to search for this signal, but would require significant measurement time. Additionally, confirming the presence of excess noise due to the diminutive geotropic fluctuations using a single interferometer with homodyne readout requires precise and stable calibrations of the shot noise level, which are difficult to achieve.

3.c. Photon Counting

GQuEST will use the recently proposed technique of single-photon signal sideband readout [28], also called photon counting, to bypass the quantum shot-noise limit (i.e. the SQL) and achieve unprecedented sensitivities within relatively short measurement times. The photon counting method works by filtering the output light of the interferometer such that single photons carrying the signal of interest can be detected. This detection scheme outperforms homodyne readout, which is quantum shot noise limited, in the detection of stochastic signals.

To explain the advantage of photon counting as proposed for the GQuEST experiment, we start by considering operating an IFO at perfect destructive interference. In this case, there is no local oscillator light at the output port of the IFO; any light observed at the output implies either the presence of a signal or the presence of some fluctuation that perturbs the interferometer arms. If the quantum gravity signal is weak and the classical noise is negligible, one may count single signal photons exiting the output port.

The geotropic length fluctuations produce effective differential interferometer arm length fluctuations $\langle \delta L_{12}^2 \rangle \equiv \langle (\delta L_1 - \delta L_2)^2 \rangle$, where $\delta L_1, \delta L_2$ are the effective length changes of the two individual arms; this is not exactly equal to Eq. (2), as that expression gives the RMS fluctuation for measuring a single length, rather than the RMS fluctuation of a differential length measurement of two nearby arms. A change in the differential arm length produces a proportional change in the flux of photons \dot{N} at the output port, with a constant of proportionality [28]

$$G \equiv \frac{\partial \dot{N}}{\partial \langle \delta L_{12}^2 \rangle} = \frac{kP_{\text{BS}}}{\hbar c}, \quad (8)$$

called the optical gain of the interferometer. The differential arm length changes due to geotropic fluctuations thus producing a signal photon flux \dot{N}^ϕ at the output port given by

$$\dot{N}^\phi = G \langle \delta L_{12}^2 \rangle = \frac{kP_{\text{BS}}}{\hbar c} \langle \delta L_{12}^2 \rangle \quad (\text{photons} \cdot \text{s}^{-1} = \text{Hz}). \quad (9)$$

This total signal photon flux cannot yet be evaluated unequivocally using e.g. Eq. (2), as the PSD of the pixellon ϕ signal falls off as $1/f$ (see Fig. 1), and therefore its integral ($\langle \delta L_{12}^2 \rangle \equiv \int S_L^\phi(f) df$) diverges logarithmically. This can be attributed to the lack of a high-frequency (UV) cut-off in the pixellon theory which further theoretical development should resolve. We evaluate the total photon flux of the signal within some finite detection bandwidth by integrating over the photon flux spectral density; this flux spectral density is

$$S_N^\phi(\epsilon) = G \frac{S_L^\phi(f)}{2} = \frac{S_L^\phi}{4\bar{S}_L^q} \quad \text{for } \epsilon = \pm f; \quad (10)$$

this quantity represents the frequency decomposition of the signal sideband photon flux as a *two-sided* spectral density. We use the two-sided spectral density to evaluate the photon flux, as geotropic signals of frequency f produce signal sidebands at optical frequencies $\nu - f$ and $\nu + f$ which can be separately measured. For this reason, we specifically use ϵ to denote measurements at an optical frequency shift $-\nu < \epsilon < \infty$, to distinguish it from measurements at signal frequency $0 < f < \infty$. The last equality in Eq. (10) is obtained from relating the optical gain to the shot noise level as $\bar{S}_L^q = \frac{1}{2} \cdot G^{-1}$, which expresses that the vacuum state of the electromagnetic field (with an expectation value of $\frac{1}{2}$ quanta) produces spurious displacement signals \bar{S}_L^q in the output of the interferometer.

To show the effectiveness of photon counting, we evaluate the signal photon flux due to geotropic fluctuations in a range of frequencies Δf above and below the laser source frequency:

$$\dot{N}_{\text{peak}}^\phi = \int_{-\Delta f}^{\Delta f} S_N^\phi(\epsilon) d\epsilon = \alpha \mathcal{O}(1) \text{ Hz} \left(\frac{P_{\text{BS}}}{10 \text{ kW}} \right) \left(\frac{L}{5 \text{ m}} \right). \quad (11)$$

For a measurement where photons are counted over an interval dt , the number of accumulated signal photons is $dN = \dot{N} dt$. The variance of the number of accumulated photons σ_{dN}^2 is determined by Poisson statistics, therefore $\sigma_{dN}^2 = dN$. Thus, when counting signal photons in an IFO operated at perfect destructive interference without any classical noise, the SNR accumulates over time as

$$\text{SNR}_{\text{count}}^2 = \int_0^T \frac{(dN_{\text{peak}}^\phi)^2}{dN_{\text{peak}}^\phi} = \int_0^T \dot{N}_{\text{peak}}^\phi dt \approx T \Delta f \frac{\bar{S}_L^\phi}{2\bar{S}_L^q}, \quad (12)$$

$$\approx \alpha \left(\frac{T}{0.25 \text{ s}} \right) \left(\frac{P_{\text{BS}}}{10 \text{ kW}} \right) \left(\frac{L}{5 \text{ m}} \right), \quad (13)$$

where we approximate the spectrum as a constant equal to the peak value over the bandwidth of the signal Δf . For this approximation, we use our definition of Δf as for the homodyne readout scheme above, rather than making the approximation exact by redefining the bandwidth (which would be necessary to account for the different powers of S_L^ϕ in the integrands of Eqs. (6) and (12)).

Comparing Eqs. (6) and (12) indicates that reading out the interferometer by counting individual signal-carrying

photons is fundamentally and profoundly more efficient than the usual homodyne readout. Under ideal conditions, it requires less than a second to detect geotropic fluctuations with $\alpha = 1$ at 1σ significance and even a 3σ to 5σ test of the theory would take less than a minute.

In practice, this sensitivity cannot be achieved with current technology, as a realistic interferometer cannot be operated at perfect destructive interference for many reasons. There will always be small amounts of light at the output port of the interferometer due to imperfections in the optics and low-frequency length perturbations of the arms. These small amounts of light, also known as contrast defects, constitute a photon flux many orders of magnitude greater than the signal in Eq. (9) and would obscure it.

However, the condition of having no local oscillator or contrast defect light at the output can be emulated by filtering the light at the output port, removing unwanted optical power. This exploits the fact that the frequencies of the output optical field carrying the signal (the signal sideband) are different from the frequencies of the optical field from both the input laser and much of the classical noise. GQuEST will use optical cavities to strongly filter the output light, letting through only photons with frequencies corresponding to the desired signal.

We can model the effect of the cavities as a band-pass filter function $F(\epsilon - \epsilon_r)$, where ϵ_r is the readout frequency, which is set by choosing the resonant frequency of the cavities to be at a detuning ϵ_r from the carrier, and $0 < F \leq 1$, where $F(0) \approx 1$, $F(-\epsilon_r) \ll 1$, and the pass-band bandwidth $\Delta\epsilon \approx 25 \text{ kHz}$ (c.f. Appendix A.9). By choosing $\epsilon_r = +f_{\text{pk}}$, signal photons at sideband frequencies $(f_{\text{pk}} - \Delta\epsilon/2) < \epsilon < (f_{\text{pk}} + \Delta\epsilon/2)$ are transmitted through the optical filter cavities, and photons at different sideband frequencies are rejected. The filtered signal photon flux is then

$$\begin{aligned} \dot{N}_{\text{pass}}^\phi &= \int_{-\nu}^{\infty} S_N^\phi(\epsilon) F(\epsilon - \epsilon_r) d\epsilon = \int_{\epsilon_r - \Delta\epsilon/2}^{\epsilon_r + \Delta\epsilon/2} S_N^\phi(\epsilon) d\epsilon \approx \frac{\Delta\epsilon \bar{S}_L^\phi}{4\bar{S}_L^q} \\ &\approx \alpha 1.4 \cdot 10^{-3} \text{ Hz} \left(\frac{P_{\text{BS}}}{10 \text{ kW}} \right) \left(\frac{L}{5 \text{ m}} \right)^2 \left(\frac{\Delta\epsilon}{25 \text{ kHz}} \right), \quad (14) \end{aligned}$$

which is valid for the realistic case that the readout bandwidth $(\epsilon_r - \Delta\epsilon/2) < \epsilon < (\epsilon_r + \Delta\epsilon/2)$ is chosen near the peak of the signal and $\Delta\epsilon \ll \Delta f$. The output flux in Eq. (14) only considers photons due to the signal in Eq. (3); in Section 4 we expand on the design of the experiment, including filter cavities to enable photon counting readout, and then evaluate the experimental sensitivity with the presence of noise in Section 4.g.

4. EXPERIMENTAL DESIGN

The interferometer diagram in Fig. 2 indicates the essential elements of the GQuEST IFO design. The fiducial design parameters for the GQuEST IFOs are summarized

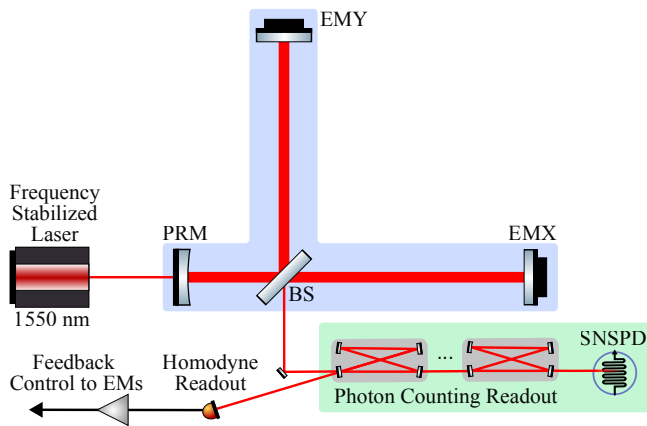


FIG. 2. Simplified diagram of the experimental design for one GQuEST interferometer (IFO). Light from a frequency-stabilized laser with a wavelength of 1550 nm is incident on the beamsplitter (BS) of the power-recycled IFO. The input laser light is transmitted through the power-recycling mirror (PRM), which together with the end mirrors (EMX, EMY), form the power-recycling cavity. The output light of the IFO is filtered through four narrowband filter cavities, which provide > 200 dB of suppression of light at the laser frequency. Photons that pass through the filter cavities are detected using a superconducting nanowire single-photon detector (SNSPD). The light reflected off the first filter cavity is used in a homodyne readout scheme to enable feedback control of the IFO.

in Table I. The estimated noise separated into contributions from various sources is shown in Fig. 3.

4.a. Interferometer Design

The IFO arm length is chosen to be 5 meters, which balances the increase of the signal strength for longer arms ($\overline{S}_L^{\phi} \propto L^2$) with technical constraints on photon counting that favor having the peak of the signal spectrum at higher frequencies (note $f_{\text{pk}} \propto 1/L$, Eq. (4)), as discussed in Section 4.g. We set the IFO arm angle $\Theta = 90^\circ$ for simplicity, as the increase in the signal magnitude using larger angles is not substantial. We use a laser wavelength of $\lambda = 1550$ nm to enable the use of silicon optics; silicon has favorable properties for the suppression of noise, as argued below, but is opaque to light of shorter conventional wavelengths such as 1064 nm. The use of silicon also takes advantage of the continuing development of optics for this wavelength for future gravitational-wave detectors [32].

The interferometer is operated near destructive interference, allowing only a small fraction of the total power on the beamsplitter to be directed toward the output port. The remainder returns toward the input laser. Between the input laser and the beamsplitter, a power-recycling mirror is added, which forms a resonant cavity with the arm end mirrors (see Fig. 2). This power-recycling cavity enhances the injected laser power of 10 W to 10 kW or more of circulating light.

Low-frequency perturbations of the interferometer arms from the environment need to be counteracted to maintain the IFO at its operating point. This is done with feedback control, where the perturbations are read out by measuring modulations of the output field reflected off the first filter cavity (i.e. homodyne readout of the output power, see Fig. 2 and Appendix A.3).

The target output light power due to low-frequency perturbations and differential imperfections (i.e. the contrast defect) is $P_{\text{out}} = \mathcal{O}(100)$ mW, which is small compared to the power on the beamsplitter but large compared to the expected photon flux due to the geontropic signal. The following design elements enable the signal to be detected despite the presence of non-signal-carrying contrast defect light and other noise.

4.b. Filter Cavities

To suppress the contrast defect light, we will use a series of narrowband optical filter cavities at the interferometer output that resonantly transmit light at a frequency $\nu + \epsilon_r$ (where ν is the frequency of the input laser and ϵ_r is the signal sideband frequency). Based on the signal PSD in Section 2.a and the estimated noise PSD in Fig. 3 (see Section 4.f), we choose a filter cavity offset frequency of $\epsilon_r = 17.6$ MHz, with a filter FWHM bandwidth of 42 kHz (and a cavity pole of 21 kHz). Each of the four filter cavities thus provides roughly $20 \log(17.6 \text{ MHz}/21 \text{ kHz}) = 58$ dB of power suppression of the carrier light for a total of 232 dB of filtering, which reduces as much as 1 W of light at carrier frequency to a level below that of the signal. With multiple filters in series, the effective pass bandwidth is $\Delta\epsilon \approx 25$ kHz. During operation, the value of ϵ_r can be varied almost arbitrarily, but sufficient filtering is expected to be achievable primarily in the range from 8 to 40 MHz (see Appendix A.9). Changing ϵ_r allows the frequency dependence of the signal PSD to be resolved; this also enables the noise spectrum to be characterized.

4.c. Single-Photon Detection with SNSPDs

Photons will be detected downstream of the filter cavities using superconducting nanowire single-photon detectors (SNSPD). SNSPDs have been demonstrated to achieve 98% detection efficiency at 1550 nm [33] and intrinsic dark count rates (i.e. the rate of spurious SNSPD signals in the absence of light) as low as $6 \cdot 10^{-6}$ counts per second (cps) [34].

These detectors are fabricated by patterning thin (≈ 5 nm) films of superconductors (typically WSi, MoSi, NbN, or NbTiN) into nanowires in the region of 100-250 nm in width. This nanowire is meandered to cover the active area, where $20 \times 20 \mu\text{m}$ is large enough to couple efficiently to a single optical mode at 1550 nm. To ensure high absorption in the device, the meandered nanowire is embedded into a dielectric stack, with either a metal [35]

or dielectric [33] back-reflector. The superconducting nanowire is current-biased at a high fraction of its critical depairing current such that the absorption of the single 1550 nm photon is sufficient to break the superconductivity across the whole nanowire, through a highly nonlinear process [36, 37]. The resistive domain in the nanowire re-diverts the original current into a readout amplifier, providing a digital ‘click’ to register the photon detection event, referred to as a ‘count’.

While SNSPDs can have low intrinsic background count rates and high quantum efficiency using the techniques above, they must be optimized for use with an interferometer experiment. To maintain such low background count rates requires the output of the interferometer to be efficiently coupled to the SNSPD while preventing any spurious photons (e.g. from a thermal background) from producing counts in the detector. To reduce the thermal background, the optical fiber that carries the output photons to the SNSPD will be shrouded and cooled. In addition, a free-space coupling of the interferometer output to the SNSPD in a cryogenic environment might be required, although free-space coupled dark count rates of 10^{-2} cps have already been demonstrated for a $\lambda = 1550$ nm SNSPD readout [38].

4.d. High Optical Powers

The principal advantage of the photon counting readout is the elimination of quantum noise from the interferometric SQL (see Eq. 5). In the absence of this noise, the dominant noise encountered in the experiment is expected to be classical noise from thermal fluctuations in the optics.

An important means to mitigate this noise is the choice of optical substrate material. GQuEST will use crystalline silicon optics, instead of the fused silica used in other precision laser interferometers (e.g. LIGO, Holometer). Silicon has a higher thermal conductivity, a higher phonon propagation speed, and a higher mechanical quality factor than fused silica (at the operating temperature). These contribute to the reduction of different kinds of thermal noise (see the Appendix) [39]. Although silicon’s absorption of light with a wavelength of 1550 nm is greater than the absorption of fused silica at 1064 nm, this effect is negligible as the total absorption in the optics is dominated by absorption in the optical coatings.

In particular, the use of crystalline silicon mitigates thermal lensing in the beamsplitter. Absorption of the light traversing the beamsplitter creates a temperature gradient inside the substrate, which causes inhomogeneous refraction due to the temperature dependence of the index of refraction. This effect, known as thermal lensing, scatters light power from the fundamental Gaussian input mode into higher-order modes (see Appendix A.7) when the light is transmitted through the beamsplitter. The resulting differential scattering between the arms perturbs the destructive interference at the output, creating a contrast defect. The contrast defect produces spurious output light

at the carrier frequency that requires suppression by the filter cavities. If the fractional power leakage due to the contrast defect is large compared to the transmission of the power-recycling mirror, then it also limits the amount of power that can be built up in the interferometer.

4.e. Laser Noise

The output filter cavities will remove the carrier light at frequency ν , but the input laser light will also carry noise spanning a range of frequencies. In addition to a 250 Hz laser linewidth, the input laser’s spectrum has a white noise floor due to amplified spontaneous emission equivalent to a laser phase noise on the order of 10^{-7} rad/ $\sqrt{\text{Hz}}$ [32]. This would amount to a photon flux of $\dot{N}_{\text{pass}}^{\text{LP}} = \mathcal{O}(10^8)$ Hz at the detector (after the readout filter cavities, see Appendix A.1), which is far greater than the signal photon flux and therefore requires suppression. An input filter cavity (which is elided and considered a part of the source in Fig. 2) and the power-recycling cavity will each have a bandwidth $\mathcal{O}(10)$ kHz, and therefore each provides a power suppression of $\mathcal{O}(60)$ dB at the signal peak frequency for a total of $\mathcal{O}(120)$ dB of filtering of the laser amplitude and phase noise. The suppressed laser noise photon flux is thus expected to be $\dot{N}_{\text{pass}}^{\text{LP}} = 10^{-4}$ Hz, which is negligible compared to the photon flux of the signal, calculated in Section 4.g.

4.f. Thermal Noise

Sideband photons from the interferometer not due to the signal with frequencies in the filter passband ($\epsilon \approx \epsilon_r$), will be detected as noise on the photodetector. The dominant source of such noise sidebands is expected to be thermal excitations of the optics, which couple to the circulating light in different ways.

Mechanical elastic resonances of the optical substrates entail oscillations of the reflecting surfaces of the optics. This produces significant noise sidebands at the frequency of the mechanical mode, with a width depending on the quality factor of the resonance. We have modeled this mechanical noise analytically and numerically and find that for thin, disc-like mirrors, the mechanical modes (which we refer to as ‘solid normal modes’) create a spectrum of noise peaks that are regularly spaced across the signal band, as plotted in Fig. 3 (see Appendix A.4 a) [19]. The spacing of the peaks, at our measurement frequencies, is determined by the speed of sound of (longitudinal) P-waves in the material. The impact of these peaks is mitigated through the narrow bandwidth of the filter cavities: the filter passband is chosen to lie between successive mechanical resonances (see Fig. 3).

The optical coatings applied to the substrates entail additional thermal noise and we have modeled this effect (see Appendix A.4 b); the dominant contribution from coating thermal noise is expected to be its lowering of

the total mechanical quality factor of the optics. Unlike previous modeling of coating thermal noise [40], which has implicitly only considered the frequency regime below the first mechanical eigenfrequency of the optics, this new model is applicable for frequencies in our readout band. Based on our model, it is expected the total mechanical noise (MN) (including substrate and coating) is the dominant contribution to the total classical noise, i.e. $S_L^{\text{MN}} \approx S_L^c = \left(5 \cdot 10^{-22} \text{ m}/\sqrt{\text{Hz}}\right)^2$. For the reference sensitivity and measurement time estimates considered below, we therefore use a conservative reference level of $\bar{S}_L^c = (10^{-21} \text{ m}/\sqrt{\text{Hz}})^2 > S_L^c$.

Notably, the classical noise level is expected to be above the signal level, which implies a nonzero background photon count rate. Therefore, the sensitivity of the experiment will be limited both by the low flux of signal photons and by the variance of the flux of photons from thermal noise. The statistical impact and an experimental strategy to remove this noise are described in Section 4.g and Section 4.h, respectively.

TABLE I. Parameters of the fiducial GQuEST design. The noise spectral densities are evaluated at 17.6 MHz.

parameter	symbol	value
Geotropic fluct. scale parameter	α	$\mathcal{O}(1)$
IFO arm length	L	5 m
Power on beamsplitter	P_{BS}	10 kW
Laser wavelength	λ	1550 nm
Laser frequency	ν	193.4 THz
Nominal filter offset frequency	ϵ_r	17.6 MHz
Filter bandwidth	$\Delta\epsilon$	20 kHz
Twin IFO separation	L_{sep}	1.5 m
IFO inter-arm angle	Θ	90°
Signal spectral density (peak)	\bar{S}_L^ϕ	$(3 \cdot 10^{-22} \text{ m}/\sqrt{\text{Hz}})^2$
Thermal noise spectral density	\bar{S}_L^c	$(10^{-21} \text{ m}/\sqrt{\text{Hz}})^2$
Shot noise spectral density	\bar{S}_L^q	$(6 \cdot 10^{-19} \text{ m}/\sqrt{\text{Hz}})^2$
Filtered signal photon flux	$\dot{N}_{\text{pass}}^\phi$	$1.4 \cdot 10^{-3} \text{ Hz}$
Filtered classical noise photon flux	\dot{N}_{pass}^c	$1.6 \cdot 10^{-2} \text{ Hz}$
Photon detector dark count rate	\dot{N}^d	$< 10^{-3} \text{ Hz}$
Observation time for 5σ test for $\alpha = 1$	T	$\mathcal{O}(10^5) \text{ s}$

4.g. Reference Sensitivity

To make a realistic estimate of the sensitivity of the interferometers, we have to evaluate the signal count rate, $\dot{N}_{\text{pass}}^\phi$, the count rate from classical interferometer noise, \dot{N}_{pass}^c and the dark count rate of the photodetector, \dot{N}^d .

The filtered photon flux from classical noise is computed similarly to the computation of the filtered signal photon flux (see Eq. (10) and Eq. (14)), where we substitute S_L^ϕ for the classical displacement spectral density S_L^c . In addition,

for both the signal and the noise, we model the frequency dependence of the transmission of the optical filter cavities as the filter function $F(\epsilon - \epsilon_r)$. The filtered classical noise photon flux is then

$$\dot{N}_{\text{pass}}^c = \int_{-\infty}^{\infty} S_N^c(\epsilon) F(\epsilon - \epsilon_r) d\epsilon \approx \frac{\Delta\epsilon \bar{S}_L^c}{4\bar{S}_L^q} \quad (15)$$

$$\approx 1.6 \cdot 10^{-2} \text{ Hz} \left(\frac{P_{\text{BS}}}{10 \text{ kW}} \right) \left(\frac{\Delta\epsilon}{25 \text{ kHz}} \right), \quad (16)$$

which scales linearly with the expected classical noise level $\bar{S}_L^c = (10^{-21} \text{ m}/\sqrt{\text{Hz}})^2$ (see Appendices A.4 a and A.4 b). in the nominal readout bandwidth $\Delta\epsilon$ centered on the signal peak. The SNR can then be found by considering that the signal accumulates as $\int dt \dot{N}^\phi$, while the total variance is the quadrature sum of all noise count rate contributions, i.e. $\sigma_{dN}^2 = \sum_i \sigma_{dN^i}^2$, integrated over time. This leads to an SNR of

$$\text{SNR}_{\text{counting}}^2 = \int_0^T \frac{(\dot{N}_{\text{pass}}^\phi dt)^2}{(\dot{N}_{\text{pass}}^\phi + \dot{N}_{\text{pass}}^c + \dot{N}^d) dt} \quad (17)$$

This can be evaluated as [28]

$$\text{SNR}_{\text{counting}}^2 \approx \frac{T\Delta\epsilon \bar{S}_L^\phi}{4 \bar{S}_L^q} \left(1 + \frac{\bar{S}_L^c}{\bar{S}_L^\phi} + \frac{4\dot{N}^d \bar{S}_L^q}{\Delta\epsilon \bar{S}_L^q} \right)^{-1} \quad (18)$$

If the dark count rate and classical noise were negligible, the SNR is estimated to be

$$\begin{aligned} \text{SNR}_{\text{counting}}^2 &\approx \frac{T\Delta\epsilon \bar{S}_L^\phi}{4 \bar{S}_L^q} \\ &\approx \alpha \left(\frac{T}{730 \text{ s}} \right) \left(\frac{P_{\text{BS}}}{10 \text{ kW}} \right) \left(\frac{L}{5 \text{ m}} \right)^2 \left(\frac{\Delta\epsilon}{25 \text{ kHz}} \right). \end{aligned} \quad (19)$$

Here, the increase in the required measurement time compared to Eq. (12) is due to the reduced bandwidth of the readout filter cavities compared to the full signal bandwidth.

If we realistically incorporate that the classical noise is not negligible and is larger than the expected signal level ($\bar{S}_L^c > \bar{S}_L^\phi$), and additionally assume the dark count rate is negligible compared to the classical noise ($\dot{N}^d \ll \dot{N}^c$), the SNR is given by

$$\text{SNR}_{\text{counting}}^2 \approx \frac{T\Delta\epsilon (\bar{S}_L^\phi)^2}{4 \bar{S}_L^q \bar{S}_L^c} \quad (21)$$

$$\approx \alpha^2 \left(\frac{T}{8500 \text{ s}} \right) \left(\frac{P_{\text{BS}}}{10 \text{ kW}} \right) \left(\frac{L}{5 \text{ m}} \right)^4 \left(\frac{\Delta\epsilon}{25 \text{ kHz}} \right). \quad (22)$$

From Eq. (21), we can infer that at the design sensitivity, GQuEST will be able to probe values of $\alpha < 0.6$ at 3σ significance in 60 hours of measurement time, which is the current experimental constraint set by the Holometer

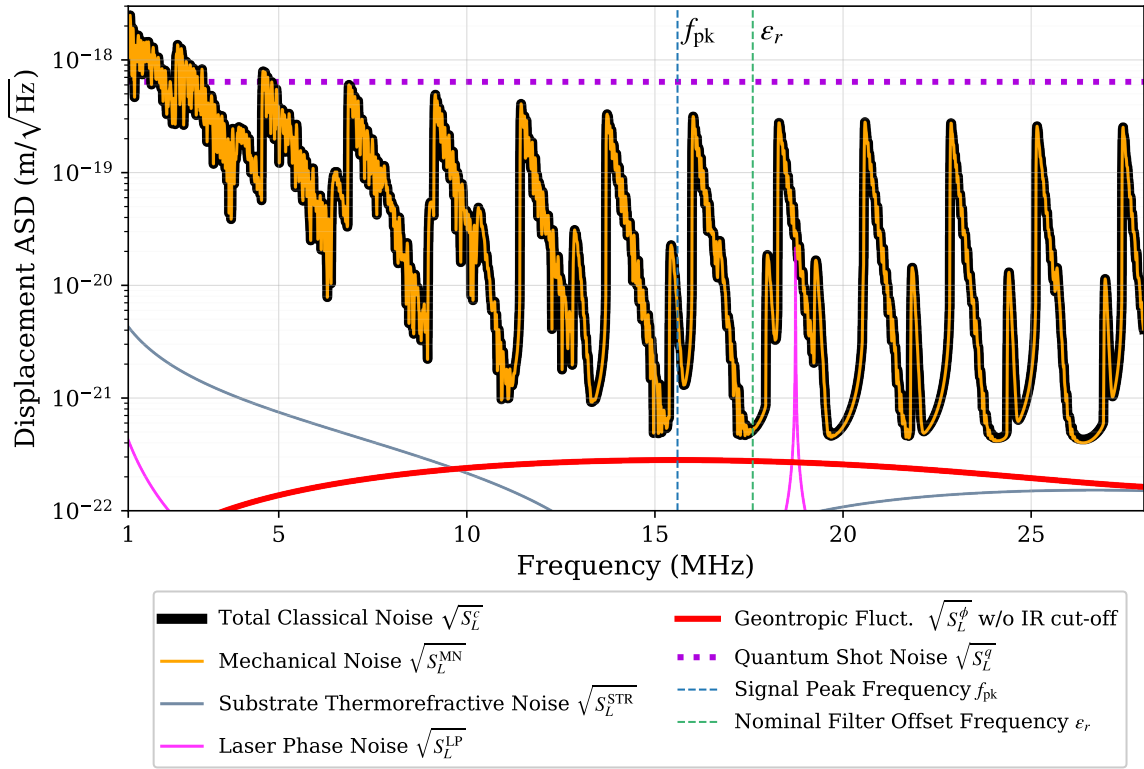


FIG. 3. The displacement amplitude spectral density of various dominant noises as estimated for the fiducial design (see Table I) are plotted together with the expected signal from geotropic quantum space-time fluctuations $\sqrt{S_L^\phi}$ (red). The total classical noise $\sqrt{S_L^c}$, which limits the sensitivity of GQuEST, and its contributions are shown (orange, gray, and pink). The various noise contributions are considered in detail in the Appendix. The standard quantum limit from shot noise $\sqrt{S_L^q}$, which GQuEST is not subject to thanks to its photon counting readout, is also shown (purple dotted line). The dark blue vertical dashed line marks the peak signal frequency f_{pk} . The green vertical dashed line marks the fiducial cavity offset frequency ϵ_r ; note that the filter bandwidth $\Delta\epsilon = 25$ kHz is narrower than the thickness of that line in this plot. See Fig. 5 in the Appendix for additional noise sources.

for geotropic fluctuations with IR cut-off. GQuEST can reach $\alpha < 0.1$ at 3σ in 2160 hours, which allows it to go beyond the current LIGO constraint on the theory without IR cut-off.

The estimate of the detection statistic using a realistic photon-counting interferometer as given by Equation (21) is a key result of this work. It should be compared against the detection statistic for homodyne (DC or ‘fringe’) readout as given by Eq. (6), and the detection statistic offered by an ideal photon-counting interferometer in Eq. (19). The rate of accrual of statistical power for a realistic photon-counting interferometer is proportional to $(4\bar{S}_L^q \bar{S}_L^c)^{-1}$, whereas the rate for homodyne readout is proportional to $(\bar{S}_L^q)^{-2}$. The factor of 4 appears in part from using only the positive component of the two signal sidebands and in part from the signal arising in only one of two optical quadratures. We note that the factor \bar{S}_L^q that appears in Eq. (21) represents the optical gain $G = (2\bar{S}_L^q)^{-1}$, which establishes the rate that signal information is extracted as photons, while the factor \bar{S}_L^c represents how

classical background noise statistically slows the extraction of signal information.

Thus, three major ways to increase the sensitivity and decrease the required measurement time are to reduce the classical noise, increase the circulating laser power, or increase the arm length. The circulating laser power is set by engineering limits, as detailed in Appendix A.2 and Appendix A.7. Increasing the arm length has the effect of shifting the peak signal frequency to lower frequencies (see Eq. (4)). Importantly, at lower frequencies, the dominant classical noises will be stronger, as the thermal noise of the optics scales as $1/f$. Additionally, a subdominant noise source might become of influence at lower frequencies; thermorefractive noise has a $1/f^2$ frequency dependence. Moreover, the achievable carrier power isolation is smaller at lower frequencies, as this suppression scales as $1/f^8$ (for the fiducial design using four readout filter cavities). At sufficiently low frequencies, the mechanical noise of the mirrors is no longer concentrated at specific frequencies, see Fig. 3, which means the noise PSD no longer exhibits significant local minima that make for suitable readout frequencies. For these reasons, a design with 5-m arms is

chosen to balance the signal magnitude and classical noise levels at the signal peak.

4.h. Coherent Signal Detection in Twin Interferometers

The dominant classical noise produces a greater photon flux than the geotropic fluctuation signal. Therefore, measurement of the underlying signal requires the subtraction of the classical noise. Using a single interferometer, this subtraction requires accurate characterization of the noise floor. Specifically, the expected photon flux in the absence of signal must be quantified with an uncertainty smaller than the magnitude of the signal. Moreover, the total classical noise needs to be measured such that the observed noise is independent of the signal and yet is representative of the noise that would be observed if the signal were present.

For the quantum space-time fluctuations we consider, the signals measured in two co-located interferometers are highly coherent, while the dominant noise is incoherent. This opens the possibility of using two interferometers to separate the correlated signal from the uncorrelated noise. This avoids the aforementioned challenges involved in removing backgrounds from the detected signal power.

An established method for doing this is to cross-correlate two co-located interferometers that use homodyne readout. In this method, a product of the electronic photodetector signals of the two interferometers is taken to compute the cross-correlation, which represents a direct estimate of the coherent signal magnitude [41, 42]. Cross-correlation therefore provides a great practical advantage and improves the required integration time of Eq. (6) by a factor 2 [28] from the use of two instruments. However, the homodyne readout method is subject to the standard quantum limit from shot noise, and this cross-correlation method does not achieve the fast detection times that photon counting provides (Eq. (21)).

When using a photon counting readout, the phase information of the optical field is lost after the detection of individual photons. Therefore, to exploit the coherence of the signals, the phase of the optical fields coming out of the two interferometers must be compared before the detection is made.

Coherent signal detection with twin GQuEST interferometers will be done using the setup shown in Fig. 4. The output light of two IFOs interferes on a beamsplitter, such that a coherent signal common to both input ports of the beamsplitter interferes constructively towards one readout port and destructively in the other. Incoherent optical fluctuations from background noise in the two IFOs will be split equally (on average) between the beamsplitter outputs. Therefore, any counts detected downstream of the beamsplitter output that contains only uncorrelated noise (the null channel) can be subtracted from the counts measured downstream of the other port (the signal channel). The difference between the null and signal channels converges to the expectation value of the correlated photon

flux through time-averaging of the measurement and thus provides a direct estimate of the geotropic signal.

Which output port contains the signal depends on the relative optical path lengths from the two interferometers to the beamsplitter, and this can therefore be selected and switched as desired. This avoids the need to build two separate readout setups with filter cavities and SNSPDs downstream of the beamsplitter, as the signal and null channels can be characterized separately at different times. The stationarity of the noise can be tested by appropriately alternating between sum and null channels. By using two interferometers, the detection statistic improves by a factor of 2 in principle, but this advantage is lost when using only one of the two output ports of the beamsplitter that combines their signals.

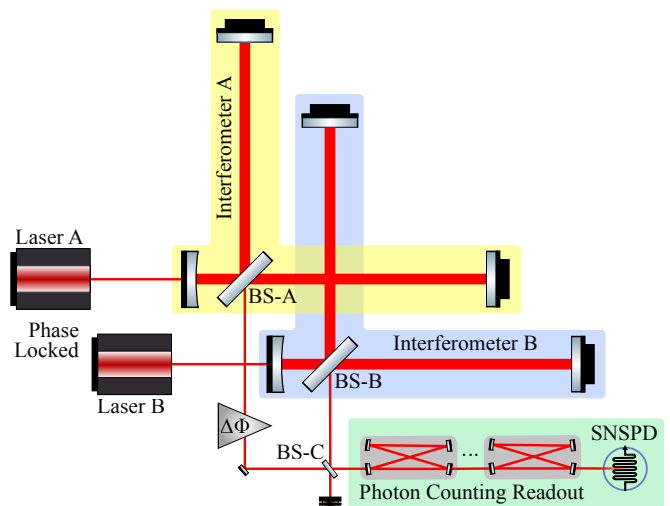


FIG. 4. Simplified schematic for the twin-interferometer (IFO) configuration of GQuEST. The outputs of two identical co-located IFOs are combined such that signals that are correlated between the IFOs interfere constructively in one output port of beamsplitter BS-C and destructively in the other. Thus, a ‘signal’ and a ‘null’ readout channel can be created and swapped by adjusting the relative phase $\Delta\Phi$ of the two IFO outputs. To ensure the output signal is coherent, the two input lasers must be coherent (phase-locked).

5. EXPERIMENTAL STAGES & OPERATIONS

The final experimental stage of GQuEST will consist of taking data from two cross-correlated interferometers with the photon counting readout described above. This ultimate experimental configuration of two high-power interferometers will require considerable development that can be staged to demonstrate the requisite technologies, performance, and integration requirements needed to achieve our experimental goals. This is the preferred approach, as this experiment is likely to be limited by classical noises in frequency and magnitude regimes outside of those previously studied by the interferometry community.

5.a. Single 0.5-m Interferometer

We will initially operate a single IFO with $L \approx 0.5$ m to rapidly test the design and to commission and characterize a high-power interferometer with the series of readout cavities and the SNSPD. This interferometer does not have the sensitivity to detect a quantum gravity signal due to its short arm length but will allow us to tackle the experimental challenges detailed in the Appendix. The goal of this experimental stage is to characterize the classical noise floor and achieve low photon count rates with an SNSPD in the absence of a detectable quantum gravity signal.

5.b. Single 5-m Interferometer

Having achieved sufficiently low noise levels in the 0.5-m interferometer phase, we will extend the arms of the interferometer, which increases the magnitude of the expected signal from geotropic fluctuations to a detectable level. This configuration will theoretically allow the GQuEST experiment to provide a significant detection of a quantum gravity signal using a single interferometer. The main observable of interest of the experiment is the average filtered photon flux out of the interferometer; the estimate thereof will be subject to a variance given by Poisson statistics and this estimate therefore improves with increased measurement time (see Eq. (12)). The identification of a signal in the average detected photon flux would first require the accurate subtraction of the noise level as characterized using the single 0.5-m interferometer (Section 5.a).

In case a significant excess photon flux is measured, follow-up investigations will be performed to determine if this signal is consistent with the expected signal from geotropic fluctuations. Specifically, the spectral shape of the signal can be measured by varying the filter offset frequency ϵ_r . In addition, the dependence of the amplitude of the signal on the arm length of the IFO can be verified by changing the arm length. In the future, we could also vary the inter-arm angle Θ to verify the dependence of the signal on this parameter.

In case no significant excess photon flux is detected, i.e. if the average photon flux is consistent with the known noise, a constraint can be placed on the magnitude of the signal parameterized by α .

5.c. Twin Interferometers

Once the experimental challenges have been addressed using a single IFO, a second identical IFO will be operated alongside the first. The detection of a geotropic signal through coherent signal detection of two interferometers does not require accurate characterization of the uncorrelated noise (see Section 4.h). This is advantageous as the uncertainty with which this noise level can be measured may be limited in practice, for example, due to irreducible

uncertainty in the calibration or non-stationarity of the noise.

Under the assumption that the geotropic signal is largely correlated between co-located IFOs and the noise is uncorrelated, the measurement of a statistically significant non-zero correlated photon flux (which requires time-averaging to reduce the measurement uncertainty) implies the presence of geotropic fluctuations, assuming there is no other coherent signal. Observation of such a correlated signal provides much stronger evidence than the observation of a signal in a single IFO, as the former is less likely to be spurious. Follow-up investigations of the same kind as for the single-interferometer stage can be performed to confirm the properties of the signal and rule out the possibility that the correlated photon flux is due to correlated noise, see Appendix A.11.

5.d. Future Design Upgrades

Through the accelerated accrual of detection statistics that photon counting provides, and given the practical advantage of using coherent signal detection with twin IFOs, the fiducial design as specified above is sufficient for the goal of detecting geotropic fluctuations with $\alpha = 0.1$ at 3σ in a few months. However, with this design we are performing a narrowband search for a wideband signal, thereby wasting over $(\Delta f - \Delta\epsilon)/\Delta f \approx 99.9\%$ of the signal power by rejecting it via the output filter cavities (compare Eq. (11) to Eq. (14)).

A potential upgrade to the design that would increase the signal power incident on the readout cavities is the implementation of signal recycling [43, 44]. The use of power recycling (as in the fiducial design) in addition to signal recycling is known as dual recycling. Signal recycling modifies the optical gain of the interferometer in a frequency-dependent way, i.e. $G \rightarrow G'(f)$. Signal-recycling increases the optical gain (by a factor given by the finesse \mathcal{F}_{SRC} of the signal-recycling cavity) within the bandwidth of that cavity, and reduces the optical gain outside the bandwidth. As the signal power at the photodetector in the GQuEST design is limited by the narrow readout cavity bandwidth $\Delta\epsilon < \Delta f$, the signal-recycling bandwidth can encompass the whole readout frequency band and thus boost the signal sideband power by a factor of $\min\{\mathcal{F}_{\text{SRC}}, c/(2L\Delta\epsilon)\}$ [45]. Dual recycling has been demonstrated in other experiments [46, 47], but presents operational challenges that we choose to avoid for the current GQuEST design.

Another possible design upgrade is the addition of more optical readout filter cavities in parallel to measure at more sideband frequencies simultaneously. This allows for faster characterization of the signal and classical noise by resolving different parts of their spectra simultaneously; this is therefore an alternative to signal recycling. Emerging technology in quantum memories and optical signal processing devices could provide more efficient, simpler, and multiplexed narrow-linewidth optical filters to fully extract the broadband signal.

Interferometers with low optical losses, such as GQuEST, can be made more sensitive by injecting squeezed states if homodyne readout is used [20]. However, squeezed states have a Poisson distribution of even-number photon occupation and decohere irreversibly into thermal states from any amount of optical loss, so the injection of these states will inevitably produce additional noise photons and is thus not advantageous when using photon counting. However, we anticipate that quantum enhancements in the form of state preparation can improve the sensitivity of a photon counting interferometer like GQuEST [48]. The implementation of such a technique will require significant further study and relates fundamentally to the quantum information of stochastic signals, the study of which is potentially also relevant more generally in the context of high-energy physics experiments that count particles produced through an incoherent scattering process, e.g. a search for particles that scatter from a stochastic signal field like a galactic dark matter halo.

6. SUMMARY & OUTLOOK

Geotropic space-time fluctuations would manifest in the output of an interferometer as a broadband signal at angular frequencies on the order of the light-crossing frequency c/L . Photon counting readout of an interferometer allows bypassing the standard quantum limit of interferometry at these frequencies, enabling an accelerated search for signals from geotropic fluctuations. The GQuEST experiment will implement this readout design for the first time and is expected to be limited by classical thermal noise from the interferometer optics. The experiment is projected to reach the nominal predicted geotropic signal PSD peak of $\bar{S}_L^\phi = (3 \cdot 10^{-22} \text{ m}/\sqrt{\text{Hz}})^2$ within several hours of integrated measurement time.

The detection of quantum space-time fluctuations of this magnitude would constitute the first evidence of the quantum nature of gravity. Such a detection would demonstrate two facets of quantum gravity. First, how gravity is quantized with a minimum uncertainty set by the Planck

scale [8, 9]. And, second, how such quantum fluctuations must accumulate across a light-crossing time of a causal diamond in a holographic theory of quantum gravity [6, 14]. While a UV-complete theory is not yet available, the low-energy effective theory as given by the pixellon model can readily be tested. The predicted signal from this model, the magnitude of which is parameterized by α , can be unequivocally detected or constrained. In the case of non-detection, the constraint set on α provides a concrete guide for theoretical efforts in quantum gravity. Depending on the stringency of the constraint and the theoretical predictions currently being prepared, the experimental data could rule out geotropic space-time fluctuations entirely.

The successful demonstration of photon counting readout of a laser interferometer would pave the way for future interferometry experiments to pursue this technique as a means to significantly increase their sensitivity. In particular, photon counting readout has the potential to greatly exceed the sensitivity gain offered by quantum squeezing in a homodyne readout scheme, the only other known method to go beyond quantum limits. Thus, photon counting has the potential to profoundly improve the sensitivity of all laser interferometers performing searches of signals with random components or stochastic signals defined by a spectral density. This includes those that aim to detect gravitational waves [28, 49, 50] and dark matter [51–54].

7. ACKNOWLEDGEMENTS

This article was prepared by the GQuEST collaboration using the resources of the Fermi National Accelerator Laboratory (Fermilab), a U.S. Department of Energy, Office of Science, Office of High Energy Physics HEP User Facility. Fermilab is managed by Fermi Research Alliance, LLC (FRA), acting under Contract No. DE-AC02-07CH11359. The GQuEST project is funded in part by the Heising-Simons Foundation through grant 2022-3341.

-
- [1] Y. Jack Ng and H. Van Dam, Limit to Space-Time Measurement, *Modern Physics Letters A* **09**, 335 (1994).
 - [2] G. Amelino-Camelia, Limits on the Measurability of Space-time Distances in (the Semi-classical Approximation of) Quantum Gravity, *Modern Physics Letters A* **09**, 3415 (1994), arXiv: gr-qc/9603014.
 - [3] C. J. Hogan, Measurement of Quantum Fluctuations in Geometry, *Physical Review D* **77**, 104031 (2008), arXiv: 0712.3419.
 - [4] E. P. Verlinde and K. M. Zurek, Observational signatures of quantum gravity in interferometers, *Physics Letters B* **822**, 136663 (2021).
 - [5] O. Kwon, Phenomenology of Holography via Quantum Coherence on Causal Horizons (2022), arXiv:2204.12080 [gr-qc, physics:quant-ph].
 - [6] K. M. Zurek, Snowmass 2021 white paper: Observational signatures of quantum gravity, arXiv e-prints (2022), arXiv:2205.01799 [gr-qc].
 - [7] K. M. Zurek, On vacuum fluctuations in quantum gravity and interferometer arm fluctuations, *Physics Letters B* **826**, 136910 (2022).
 - [8] E. Verlinde and K. M. Zurek, Modular fluctuations from shockwave geometries, *Phys. Rev. D* **106**, 106011 (2022), arXiv:2208.01059 [hep-th].
 - [9] T. He, A.-M. Raclariu, and K. M. Zurek, From shockwaves to the gravitational memory effect, *Journal of High Energy Physics* **2024**, 1 (2024).

- [10] D. Li, V. S. H. Lee, Y. Chen, and K. M. Zurek, Interferometer response to geotropic fluctuations, *Phys. Rev. D* **107**, 024002 (2023).
- [11] M. W. Bub, Y. Chen, Y. Du, D. Li, Y. Zhang, and K. M. Zurek, Quantum gravity background in next-generation gravitational wave detectors, *Phys. Rev. D* **108**, 064038 (2023).
- [12] T. Jacobson, Entanglement Equilibrium and the Einstein Equation, *Phys. Rev. Lett.* **116**, 201101 (2016), [arXiv:1505.04753 \[gr-qc\]](#).
- [13] H. Casini, M. Huerta, and R. C. Myers, Towards a derivation of holographic entanglement entropy, *JHEP* **05**, 036, [arXiv:1102.0440 \[hep-th\]](#).
- [14] T. Banks and K. M. Zurek, Conformal description of near-horizon vacuum states, *Phys. Rev. D* **104**, 126026 (2021), [arXiv:2108.04806 \[hep-th\]](#).
- [15] S. Gukov, V. S. H. Lee, and K. M. Zurek, Near-horizon quantum dynamics of 4D Einstein gravity from 2D Jackiw-Teitelboim gravity, *Phys. Rev. D* **107**, 016004 (2023), [arXiv:2205.02233 \[hep-th\]](#).
- [16] Y. Zhang and K. M. Zurek, Stochastic description of near-horizon fluctuations in rindler-ads, *Phys. Rev. D* **108**, 066002 (2023).
- [17] E. Verlinde and K. M. Zurek, Spacetime Fluctuations in AdS/CFT, *ArXiv191102018 Gr-Qc Physicshep-Ph Physicshep-Th* 10.1007/JHEP04(2020)209 (2019), [arXiv:1911.02018 \[gr-qc, physics:hep-ph, physics:hep-th\]](#).
- [18] A. Buikema, C. Cahillane, G. L. Mansell, et al., Sensitivity and performance of the advanced ligo detectors in the third observing run, *Phys. Rev. D* **102**, 062003 (2020).
- [19] A. Chou, H. Glass, H. R. Gustafson, C. Hogan, B. L. Kamai, O. Kwon, R. Lanza, L. McCuller, S. S. Meyer, J. Richardson, C. Stoughton, R. Tomlin, and R. Weiss, The Holometer: An instrument to probe Planckian quantum geometry, *Class. Quantum Grav.* **34**, 065005 (2017).
- [20] S. M. Vermeulen, L. Aiello, A. Ejlli, W. L. Griffiths, A. L. James, K. L. Dooley, and H. Grote, An experiment for observing quantum gravity phenomena using twin table-top 3d interferometers, *Classical and Quantum Gravity* **38**, 085008 (2021).
- [21] W. A. Christiansen, D. J. E. Floyd, Y. J. Ng, and E. S. Perlman, Limits on Spacetime Foam, *Physical Review D* **83**, 084003 (2011), [arXiv: 0912.0535](#).
- [22] E. S. Perlman, S. A. Rappaport, W. A. Christensen, Y. J. Ng, J. DeVore, and D. Pooley, New Constraints on Quantum Gravity from X-ray and Gamma-Ray Observations, *The Astrophysical Journal* **805**, 10 (2015).
- [23] Y. J. Ng and E. S. Perlman, Probing Spacetime Foam with Extragalactic Sources of High-Energy Photons, *Universe* **8**, 382 (2022), number: 7 Publisher: Multidisciplinary Digital Publishing Institute.
- [24] V. S. H. Lee, K. M. Zurek, and Y. Chen, Astronomical Image Blurring from Transversely Correlated Quantum Gravity Fluctuations, [arXiv \(2023\)](#), [arXiv:2312.06757 \[astro-ph, physics:gr-qc, physics:hep-ph\]](#).
- [25] W. Schottky, Über spontane stromschwankungen in verschiedenen elektrizitätsleitern, *Annalen der Physik* **362**, 541 (1918).
- [26] W. Schottky, M. Burkards, and A. Yesn, On spontaneous current fluctuations in various electrical conductors, *Journal of Micro/Nanolithography, MEMS, and MOEMS* **17**, 041001 (2018).
- [27] C. M. Caves, Quantum-mechanical noise in an interferometer, *Phys. Rev. D* **23**, 1693 (1981).
- [28] L. McCuller, Single-photon signal sideband detection for high-power michelson interferometers, [arXiv preprint arXiv:2211.04016 \(2022\)](#).
- [29] R. Price, Optimum detection of random signals in noise, with application to scatter-multipath communication–I, *IRE Trans. Inf. Theory* **2**, 125 (1956).
- [30] D. Middleton, On the detection of stochastic signals in additive normal noise–I, *IRE Trans. Inf. Theory* **3**, 86 (1957).
- [31] E. E. Flanagan, Sensitivity of the Laser Interferometer Gravitational Wave Observatory to a stochastic background, and its dependence on the detector orientations, *Phys. Rev. D* **48**, 2389 (1993).
- [32] F. Meylahn and B. Willke, Characterization of Laser Systems at 1550 nm Wavelength for Future Gravitational Wave Detectors, *Instruments* **6**, 15 (2022).
- [33] D. V. Reddy, R. R. Nerem, S. W. Nam, R. P. Mirin, and V. B. Verma, Superconducting nanowire single-photon detectors with 98% system detection efficiency at 1550 nm, *Optica* **7**, 1649 (2020).
- [34] J. Chiles, I. Charaev, R. Lasenby, M. Baryakhtar, J. Huang, A. Roshko, G. Burton, M. Colangelo, K. Van Tilburg, A. Arvanitaki, S. W. Nam, and K. K. Berggren, New constraints on dark photon dark matter with superconducting nanowire detectors in an optical haloscope, *Phys. Rev. Lett.* **128**, 231802 (2022).
- [35] F. Marsili, V. B. Verma, J. A. Stern, S. Harrington, A. E. Lita, T. Gerrits, I. Vayshenker, B. Baek, M. D. Shaw, R. P. Mirin, and S. W. Nam, Detecting single infrared photons with 93% system efficiency, *Nature Photon* **7**, 210 (2013).
- [36] D. Y. Vodolozov, Single-Photon detection by a dirty Current-Carrying superconducting strip based on the Kinetic-Equation approach, *Physical Review Applied* **7**, 034014 (2017).
- [37] J. P. Allmaras, A. G. Kozorezov, B. Korzh, K. K. Berggren, and M. D. Shaw, Intrinsic timing jitter and latency in superconducting nanowire single-photon detectors, *Physical Review Applied* **11**, 034062 (2019).
- [38] A. S. Mueller, B. Korzh, M. Runyan, E. E. Wollman, A. D. Beyer, J. P. Allmaras, A. E. Velasco, I. Craiciu, B. Bumble, R. M. Briggs, L. Narvaez, C. Peña, M. Spiropulu, and M. D. Shaw, Free-space coupled superconducting nanowire single-photon detector with low dark counts, *Optica* **8**, 1586 (2021).
- [39] R. X. Adhikari et al., A cryogenic silicon interferometer for gravitational-wave detection, *Classical and Quantum Gravity* **37**, 165003 (2020).
- [40] T. Hong, H. Yang, E. K. Gustafson, R. X. Adhikari, and Y. Chen, Brownian thermal noise in multilayer coated mirrors, *Physical Review D* **87**, 082001 (2013), publisher: American Physical Society.
- [41] S. M. Vermeulen, *Fundamental physics with laser interferometry*, [phd](#), Cardiff University (2023).
- [42] A. Chou, H. Glass, H. R. Gustafson, C. J. Hogan, B. L. Kamai, O. Kwon, R. Lanza, L. McCuller, S. S. Meyer, J. W. Richardson, C. Stoughton, R. Tomlin, and R. Weiss, Interferometric constraints on quantum geometrical shear noise correlations, *Class. Quantum Grav.* **34**, 165005 (2017).
- [43] B. J. Meers, Recycling in laser-interferometric gravitational-wave detectors, *Phys. Rev. D* **38**, 2317 (1988).
- [44] S. Hild, H. Grote, M. Hewitson, H. Lück, J. R. Smith, K. A. Strain, B. Willke, and K. Danzmann, Demonstration and comparison of tuned and detuned signal recycling in a large-scale gravitational wave detector, *Class. Quantum Grav.* **24**, 1513 (2007).

- [45] D. E. McClelland, An overview of recycling in laser interferometric gravitational wave detectors., *Australian Journal of Physics* **48**, 953 (1995).
- [46] S. Hild, H. Grote, J. Degallaix, S. Chelkowski, K. Danzmann, A. Freise, M. Hewitson, J. Hough, H. Lueck, M. Prijatelj, K. A. Strain, J. R. Smith, and B. Willke, DC-readout of a signal-recycled gravitational wave detector, *Classical and Quantum Gravity* **26**, 055012 (2009), 0811.3242.
- [47] D. Martynov, E. Hall, B. Abbott, et al., Sensitivity of the advanced LIGO detectors at the beginning of gravitational wave astronomy, *Physical Review D* **93**, 112004 (2016), publisher: American Physical Society.
- [48] J. W. Gardner, T. Gefen, S. A. Haine, J. J. Hope, J. Preskill, Y. Chen, and L. McCuller, Stochastic waveform estimation at the fundamental quantum limit, In *Preparation* (2024).
- [49] M. Maggiore, C. V. D. Broeck, N. Bartolo, et al., Science case for the Einstein telescope, *Journal of Cosmology and Astroparticle Physics* **2020** (03), 050.
- [50] M. Evans, R. X. Adhikari, C. Afle, et al., *A Horizon Study for Cosmic Explorer: Science, Observatories, and Community* (2021), arXiv:2109.09882 [astro-ph, physics:gr-qc].
- [51] S. M. Vermeulen, P. Relton, H. Grote, et al., Direct limits for scalar field dark matter from a gravitational-wave detector, *Nature* **600**, 424 (2021).
- [52] D. Antypas, A. Banerjee, C. Bartram, et al., *New Horizons: Scalar and Vector Ultralight Dark Matter* (2022), arXiv:2203.14915 [astro-ph, physics:hep-ex, physics:hep-ph, physics:physics, physics:quant-ph].
- [53] V. C. LIGO Scientific Collaboration, and KAGRA Collaboration, R. Abbott, T. Abbott, et al., Constraints on dark photon dark matter using data from LIGO's and Virgo's third observing run, *Physical Review D* **105**, 063030 (2022), publisher: American Physical Society.
- [54] Y. Du, V. S. H. Lee, Y. Wang, and K. M. Zurek, Macroscopic dark matter detection with gravitational wave experiments, *Phys. Rev. D* **108**, 122003 (2023), arXiv:2306.13122 [astro-ph.CO].
- [55] C. Cahillane, G. L. Mansell, and D. Sigg, Laser frequency noise in next generation gravitational-wave detectors, *Optics Express* **29**, 42144 (2021).
- [56] P. Fritschel, M. Evans, and V. Frolov, Balanced homodyne readout for quantum limited gravitational wave detectors, *Optics Express* **22**, 4224 (2014), publisher: Optica Publishing Group.
- [57] P. R. Saulson, Thermal noise in mechanical experiments, *Phys. Rev. D* **42**, 2437 (1990).
- [58] W. Yam, S. Gras, and M. Evans, Multimaterial coatings with reduced thermal noise, *Physical Review D* **91**, 042002 (2015), publisher: American Physical Society.
- [59] H. B. Callen and T. A. Welton, Irreversibility and generalized noise, *Physical Review* **83**, 34 (1951), publisher: American Physical Society.
- [60] Y. Levin, Internal thermal noise in the ligo test masses: A direct approach, *Phys. Rev. D* **57**, 659 (1998).
- [61] A. Gillespie and F. Raab, Thermally excited vibrations of the mirrors of laser interferometer gravitational-wave detectors, *Phys. Rev. D* **52**, 577 (1995).
- [62] J. Rodriguez, S. A. Chandorkar, C. A. Watson, G. M. Glaze, C. H. Ahn, E. J. Ng, Y. Yang, and T. W. Kenny, Direct Detection of Akhiezer Damping in a Silicon MEMS Resonator, *Sci Rep* **9**, 2244 (2019).
- [63] G. M. Harry, A. M. Gretarsson, P. R. Saulson, S. E. Kittelberger, S. D. Penn, W. J. Startin, S. Rowan, M. M. Fejer, D. R. M. Crooks, G. Cagnoli, J. Hough, and N. Nakagawa, Thermal noise in interferometric gravitational wave detectors due to dielectric optical coatings, *Class. Quantum Grav.* **19**, 897 (2002).
- [64] S. Gras and M. Evans, Direct measurement of coating thermal noise in optical resonators, *Physical Review D* **98**, 122001 (2018), publisher: American Physical Society.
- [65] V. B. Braginsky and S. P. Vyatchanin, Corner reflectors and quantum-non-demolition measurements in gravitational wave antennae, *Physics Letters A* **324**, 345 (2004).
- [66] B. Benthem and Y. Levin, Thermo-optic noise and thermochemical noise in the beamsplitter of the geo600 gravitational-wave interferometer, *Phys. Rev. D* **80**, 062004 (2009).
- [67] V. Braginsky, M. Gorodetsky, and S. Vyatchanin, Thermodynamical fluctuations and photo-thermal shot noise in gravitational wave antennae, *Physics Letters A* **264**, 1 (1999).
- [68] M. Evans, S. Ballmer, M. Fejer, P. Fritschel, G. Harry, and G. Ogin, Thermo-optic noise in coated mirrors for high-precision optical measurements, *Physical Review D* **78**, 102003 (2008).
- [69] V. B. Braginsky, M. L. Gorodetsky, and S. P. Vyatchanin, Thermo-refractive noise in gravitational wave antennae, *Physics Letters A* **271**, 303 (2000).
- [70] V. B. Braginsky, M. L. Gorodetsky, and S. P. Vyatchanin, Thermodynamical fluctuations and photo-thermal shot noise in gravitational wave antennae, *Physics Letters A* **264**, 1 (1999).
- [71] M. M. Fejer, S. Rowan, G. Cagnoli, D. R. M. Crooks, A. Gretarsson, G. M. Harry, J. Hough, S. D. Penn, P. H. Sneddon, and S. P. Vyatchanin, Thermoelastic dissipation in inhomogeneous media: Loss measurements and displacement noise in coated test masses for interferometric gravitational wave detectors, *Phys. Rev. D* **70**, 082003 (2004).
- [72] H. Siegel and Y. Levin, Revisiting thermal charge carrier refractive noise in semiconductor optics for gravitational-wave interferometers, *Phys. Rev. D* **107**, 022002 (2023).
- [73] F. Bruns, S. P. Vyatchanin, J. Dickmann, R. Glaser, D. Heintert, R. Nawrodt, and S. Kroker, Thermal charge carrier driven noise in transmissive semiconductor optics, *Phys. Rev. D* **102**, 022006 (2020).
- [74] K. A. Strain, K. Danzmann, J. Mizuno, P. G. Nelson, A. Rüdiger, R. Schilling, and W. Winkler, Thermal lensing in recycling interferometric gravitational wave detectors, *Physics Letters A* **194**, 124 (1994).
- [75] M. R. Ardigo, M. Ahmed, and A. Besnard, Stoney formula: Investigation of curvature measurements by optical profilometer, *Advanced Materials Research* **996**, 361 (2014), publisher: Trans Tech Publications.
- [76] L. McCuller, LIGO-t1900144-v3: Beam layout requirements imposed by wavefront actuators, (2019), LIGO Technical Note LIGO-T1900144-v3.
- [77] L. N. Bulaevskii, M. J. Graf, C. D. Batista, and V. G. Kogan, Vortex-induced dissipation in narrow current-biased thin-film superconducting strips, *Phys. Rev. B: Condens. Matter Mater. Phys.* **83**, 144526 (2011).
- [78] L. N. Bulaevskii, M. J. Graf, and V. G. Kogan, Vortex-assisted photon counts and their magnetic field dependence in single-photon superconducting detectors, *Phys. Rev. B: Condens. Matter Mater. Phys.* **85**, 014505 (2012).
- [79] H. Bartolf, A. Engel, A. Schilling, K. Il'in, M. Siegel, H.-W. Hübers, and A. Semenov, Current-assisted thermally activated flux liberation in ultrathin nanopatterned NbN superconducting meander structures, *Phys. Rev. B: Condens. Matter Mater. Phys.* **81**, 024502 (2010).

- [80] T. Yamashita, S. Miki, K. Makise, W. Qiu, H. Terai, M. Fujiwara, M. Sasaki, and Z. Wang, Origin of intrinsic dark count in superconducting nanowire single-photon detectors, *Appl. Phys. Lett.* **99**, 161105 (2011).
- [81] M. Colangelo, B. Korzh, J. P. Allmaras, et al., Impedance-Matched differential superconducting nanowire detectors, *Phys. Rev. Appl.* **19**, 044093 (2023).
- [82] R. Weiss, LIGO-T2200336-v2: Considerations of a ligo in air, (2022), LIGO Technical Note LIGO-T2200336-v2.

Appendix: Experimental Challenges and Detailed Noise Budget

In this appendix, we expand on the expected experimental challenges that must be overcome to achieve the nominal IFO design with the sensitivity presented above. These challenges are primarily related to maximizing the circulating power, increasing the number of signal photons, and minimizing non-signal light incident on the output photodetectors. We explore the specific physical effects that degrade photon counting interferometer performance. The prominence of these effects depends in part on the materials used in the interferometer. Table II contains fiducial parameters for the experimental design. Power spectral densities of the various noise contributions are plotted in Fig. 5.

A.1. Laser Noise

While laser noise is often characterized by a linewidth, a complete description requires considering the laser noise PSDs of relative intensity noise (RIN) and phase noise. Both laser noise spectra imply the presence of photons at frequencies offset from the carrier, potentially creating noise in the passband of the filter cavities. For the laser system used, amplified spontaneous emission causes both noises to have a broadband spectrally white contribution that must be suppressed or removed to prevent the signal from being obscured.

This input laser white phase noise PSD is $S_{\text{in}}^{\text{LP}} = (\mathcal{O}(10^{-7}) \text{ rad}/\sqrt{\text{Hz}})^2$ (Table II). This amounts to a photon flux spectral density of

$$\bar{S}_N^{\text{LP}} \approx 4 \cdot 10^3 \left(\frac{S_{\text{in}}^{\text{LP}}}{(10^{-7} \text{ rad}/\sqrt{\text{Hz}})^2} \right) \left(\frac{P_\nu}{100 \text{ mW}} \right) \left(\frac{0.8 \text{ eV}}{h\nu} \right) \quad (\text{A.1})$$

at all optical frequencies, where P_ν is the power of the light at the laser frequency ν . Given an output power of $P_\nu = P_{\text{out}} = \mathcal{O}(100) \text{ mW}$ and an output filter cavity bandwidth $\Delta\epsilon \approx 25 \text{ kHz}$, this noise amounts to a photon flux at the

photodetector of

$$\begin{aligned} \dot{N}_{\text{pass}}^{\text{LP}} &= \int_{-\infty}^{\infty} S_N^{\text{LP}}(\epsilon) F(\epsilon - \epsilon_r) d\epsilon \\ &\approx \Delta\epsilon \bar{S}_N^{\text{LP}} \approx 1 \cdot 10^8 \text{ Hz} \left(\frac{P_{\text{out}}}{100 \text{ mW}} \right). \end{aligned} \quad (\text{A.2})$$

This calculation assumes that the two interferometer arm lengths are exactly equal (i.e. no Schnupp asymmetry, $\Delta L_{\text{Schnupp}} = L_1 - L_2 = 0$). A nonzero $\Delta L_{\text{Schnupp}}$ can couple laser noise into the output port even on a perfect dark fringe; this effect is subdominant to the coupling through the contrast defect as given above (Eq. (A.2)) as long as $\Delta L_{\text{Schnupp}} < c/(2\epsilon_r) \sqrt{P_{\text{out}}/P_{\text{BS}}} \approx 3 \text{ cm}$ [55].

To combat this potentially large flux of amplified spontaneous emission photons (Eq. (A.2)), the seed laser and amplifier are followed by a single passive input filter cavity. This cavity has a round trip length of 4.5 m and mirrors with a transmissivity of 900 ppm, providing $\mathcal{O}(10^6)$ suppression of the phase noise power at frequencies a factor 10^3 above the cavity pole of $\mathcal{O}(10) \text{ kHz}$. The power-recycling of the IFO has a similar cavity pole, and together the two cavities thus suppress the phase noise by up to a factor 10^{12} in power, therefore reducing the laser phase noise to a level an order of magnitude below the signal photon flux.

A.2. Optical Power Recycling

We plan to have $\mathcal{O}(10) \text{ kW}$ of circulating optical power in the IFO to maximize the signal photon flux (and hence the SNR, see Eq. (21)). Maximizing the circulating power requires the minimization of optical losses inside the interferometer. Absorption or scattering inside the IFO, transmission of light through the end mirrors, and light leaving the IFO through the output port all limit the build-up of circulating power. Specifically, the circulating optical power in a power-recycling (PR) optical cavity as in Fig. 2 is [20]:

$$P_{\text{BS}} = \frac{T_{\text{PR}}}{\left[1 - \sqrt{R_{\text{PR}} R_{\text{EM}} (1 - \Lambda_{\text{tot}})} \right]^2} P_{\text{in}}, \quad (\text{A.3})$$

where the variables and their fiducial values are defined in Table II. These parameters allow the desired circulating optical power $P_{\text{BS}} = 10 \text{ kW}$ to be achieved with losses as high as $\Lambda_{\text{tot}} \lesssim 800 \text{ ppm}$, where the losses are the limiting factor for the power build-up if $\Lambda_{\text{tot}} > T_{\text{PR}}$. However, the experimental design aims to limit the total losses to $\mathcal{O}(100) \text{ ppm}$ to provide a margin for obtaining the desired circulating power.

A.3. Control of Mirror Positions

Another important part of the IFO design is the implementation of feedback control to maintain the IFO at

TABLE II. Additional parameters of the fiducial IFO design. Material parameters are evaluated at room temperature.

PARAMETER	SYMBOL	VALUE
Laser wavenumber	k	$4 \cdot 10^6 \text{ m}^{-1}$
Input laser white phase noise PSD	$\bar{S}_{\text{in}}^{\text{LP}}$	$(10^{-7} \text{ rad}/\sqrt{\text{Hz}})^2$
Nominal filter offset frequency/readout frequency	ϵ_r	17.6 MHz
Minimum practical filter offset frequency	ϵ_r^{min}	8 MHz
Maximum practical filter offset frequency	ϵ_r^{max}	40 MHz
End mirror reflectivity	R_{EM}	≥ 0.9999
Power-recycling mirror transmissivity	T_{PR}	500 ppm
Total (round-trip) fractional power loss	Λ_{tot}	$\mathcal{O}(10)$ ppm
End mirror $1/e^2$ (2σ) intensity beam radius	w	3 mm
End mirror diameter	d	25.4 mm
End mirror thickness	h	2 mm
End mirror substrate material	c-Si	294K crystalline Si
Beamsplitter $1/e^2$ (2σ) intensity beam radius	w	3 mm
Beamsplitter diameter	d_{BS}	38.1 mm
Beamsplitter thickness	h	2 mm
Beamsplitter substrate material	c-Si	294K crystalline Si
c-Si Density	ρ_s	2329 kg m^{-3}
c-Si Young's modulus	E_s	156 GPa
c-Si Poisson ratio	ν_s	0.265
c-Si body wave quality factor (at ϵ_r)	Q_s	$\mathcal{O}(10^6)$
c-Si Thermal conductivity	κ_s	$380 \text{ W m}^{-1} \text{ K}^{-1}$
c-Si Specific heat	C_s	$710 \text{ J kg}^{-1} \text{ K}^{-1}$
c-Si thermorefractive coefficient $\partial n/\partial T$ at λ	β_s	$2 \cdot 10^{-4} \text{ K}^{-1}$
c-Si Coefficient of thermal expansion	α_s	$2.5 \cdot 10^{-6} \text{ K}^{-1}$
c-Si Index of refraction at λ	n	3.48
c-Si Diffusion constant	D	$3.76 \cdot 10^{-3} \text{ m}$
c-Si Debye length	λ_{D}	$4.33 \cdot 10^{-7} \text{ m}$
c-Si Mean carrier density	N_0	$< 10^{18} \text{ m}^{-3}$
c-Si Optical absorption coefficient	α_e	$1.2 \cdot 10^{-26} \text{ m}^{-3}$
c-Si Fractional power absorption at λ	Λ_{Si}	$2 \cdot 10^{-4} \text{ m}^{-1}$
Fractional BS coating power absorption (assumed)	Λ_c	3 ppm
Fractional BS substrate power absorption	Λ_s	0.4 ppm
Coating material	-	$\text{Ta}_2\text{O}_5 - \text{SiO}_2$
Coating thickness	h_c	$\mathcal{O}(10) \mu\text{m}$
Ta_2O_5 Young's modulus	E_{Ta}	120 GPa
SiO_2 Young's modulus	E_{SiO_2}	70 GPa
Ta_2O_5 Poisson ratio	ν_{Ta}	0.29
SiO_2 Poisson ratio	ν_{SiO_2}	0.19
Coating body wave quality factor (at ϵ_r) (derived)	Q_c	1400
Coating thermal conductivity (average)	κ_c	$2.6 \text{ W m}^{-1} \text{ K}^{-1}$
Coating density (average)	ρ_c	5200 kg m^{-3}
Coating specific heat (average)	C_c	$360 \text{ J kg}^{-1} \text{ K}^{-1}$
Coating effective coefficient of thermal expansion	$\bar{\alpha}_c$	$6 \cdot 10^{-6} \text{ K}^{-1}$
Coating effective thermorefractive coefficient	$\bar{\beta}_c$	$8 \cdot 10^{-6} \text{ K}^{-1}$
c-Si Effective coefficient of thermal expansion	$\bar{\alpha}_s$	$6.4 \cdot 10^{-6} \text{ K}^{-1}$
Coating stress	σ_c	0.5 GPa
Fused silica thermal conductivity	κ_{FS}	$1.38 \text{ W m}^{-1} \text{ K}^{-1}$
Fused silica thermorefractive coefficient at λ	β_{FS}	$8.5 \cdot 10^{-6} \text{ K}^{-1}$
Fused silica fractional power absorption at λ	Λ_{FS}	10^{-4} m^{-1}

the operating point. The position of the mirrors directly influences the amount of power circulating inside the interferometer; the length of the power-recycling cavity must be controlled to be resonant with the laser light to maintain the high-power circulating field. Deviations of the positions of mirrors cause power to be lost from the cavity. Moreover, differential fluctuations of the positions of the arm end mirrors produce noise light at the output.

Environmental noise will couple to and perturb the positions of the optics. Feedback control of the differential position of the end mirrors will be implemented to counteract these perturbations. Homodyne readout can be used to measure this degree of freedom, and a homodyne readout channel is implemented using the residual fringe light power at the output P_{out} that is reflected from the first of the filter cavities (see Fig. 2, bottom left). This readout can alternatively be implemented with the balanced-homodyne scheme [56] to minimize the fringe light required to detect the length perturbation. Deviations of the mirror positions thus inferred will be fed back to the mirror positions in a control loop, where the mirrors are actuated using piezoelectric transducers.

Given a target optical loss of $\mathcal{O}(10)$ ppm from motion, we estimate (using Eq. (8)) that the maximum allowable RMS differential arm length deviation is $\Delta\langle\delta L_{12}\rangle = \mathcal{O}(1)$ nm. The end mirror actuator design is intended to achieve feedback control with a bandwidth of $\mathcal{O}(700)$ Hz, similar to the performance of the Holometer [19].

A.4. Mechanical Thermal Noise in the Optics

Thermal excitation of the optical components is expected to be a significant source of noise for the GQuEST experiment. The dominant noise source is elastic mechanical vibrations of the disc-shaped mirror substrates and of the optical coatings, known as solid normal modes (SNM) as shown in Fig. 5. In general, thermal dissipation produces fluctuations in the optics that affect the optical path length of light interacting with the optic. This section treats thermal mechanical fluctuations (i.e. vibrations). This noise source has in previous literature been referred to as ‘Brownian thermal noise’ [40, 57, 58]; we avoid the term ‘Brownian’ since the underlying physical process does not involve mass diffusion. The following section (Appendix A.5) considers inhomogeneous dissipation, which produces temperature fluctuations inside the optic that results in noise on the incident light.

We consider two methods of modeling noise from homogeneous mechanical thermal excitation of the optics. Both methods invoke the fluctuation-dissipation theorem (FDT) of Callen and Welton [59] to find the mechanical noise fluctuations conjugate to thermal dissipation. The first is the ‘direct’ method as posited by Levin, which derives the noise by considering the power dissipated by an oscillatory force on the optic. The second method derives the noise by decomposing the excitation of the optic into normal modes, and then considering these modes to be thermally

populated according to the equipartition theorem.

The ‘direct’ method proposed by Levin [60] is conventionally used in the interferometry community to model the PSD of mechanical thermal noise in the optics. In this method, one starts by considering an oscillatory force $F = F_{\text{pk}} \cos(\Omega t)$ applied to the optic surface, conceptually arising from the radiation pressure of an incident light beam. Here, Ω is the angular frequency at which the noise is to be computed (i.e. $\Omega = 2\pi f$ or $\Omega = 2\pi\epsilon$ in the side-band picture). The force produces elastic deformations of the material, which modulates the optical path length of the incident beam. This deformation stores elastic energy $U_{\text{max}} \propto F_{\text{pk}}$ in the optic, which then partially dissipates when the material relaxes. The dissipated power is $W_{\text{diss}} = \Omega U_{\text{max}}/Q$, where $Q(\Omega)$ is the quality factor of the mechanical system, which quantifies the internal damping of the material. The FDT implies that the thermal noise in a certain physical degree of freedom is determined by the dissipation occurring in response to a generalised force acting on that degree of freedom. Formally, the dissipation is quantified by the resistive part of the frequency response, i.e. the real part of the admittance $Y(\Omega)$ of the system.

Levin’s direct method thus relates the force and the dissipated energy to compute the PSD of the fluctuating deformations of the optic produced by thermal energy in the material [60]:

$$S_L^{\text{FDT}}(\Omega) = \frac{4k_B T}{\Omega} \frac{U_{\text{max}}}{Q F_{\text{pk}}^2} = \frac{4k_B T}{\Omega^2} |\text{Re}[Y(\Omega)]|, \quad (\text{A.4})$$

where the parameters are defined above or in Table II. The mechanical frequency response of the optic, when driven by radiation pressure along a Gaussian beam profile, thus provides the needed information to compute the mechanical thermal noises. The conventional analytical application of Levin’s method treats the optic as an infinite half-space of material, in which case there are no SNM resonances and the only physical scale is given by the beam width. This approach is therefore not applicable at frequencies comparable to SNM resonances, i.e. for the GQuEST measurement band. However, we use Levin’s method to calculate coating contributions to the mechanical noise, as explained in Appendix A.4 b.

The optic’s mechanical thermal noise is modeled by decomposing the mechanical excitation into normal modes of the optic, following Gillespie & Raab [61]. The noise spectrum is then given by a thermal population of these modes according to the equipartition theorem. The expected mechanical noise from SNMs, which we call the mechanical noise $S_L^{\text{MN}}(\Omega)$, as shown in Fig. 5 is modeled using this method, as we explicate below in Appendix A.4 a. Importantly, we find that the noise at frequencies between SNM resonances, i.e. the total noise $S_L^c(\epsilon_r)$, is mostly due to the effect of the optical coatings, and this contribution is quantified in Appendix A.4 b.

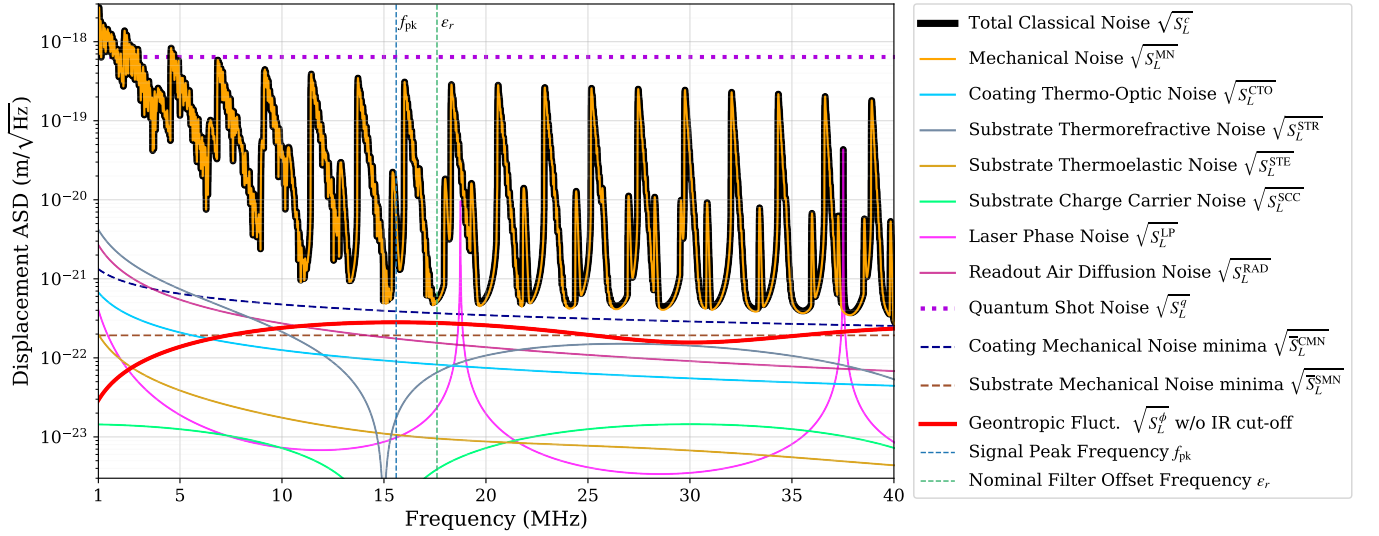


FIG. 5. The displacement amplitude spectral density of various noises as estimated for the fiducial design (see Table II) are plotted together with the expected signal from geotropic quantum space-time fluctuations $\sqrt{S_L^\phi}$ (red). The total classical noise $\sqrt{S_L^c}$, which limits the sensitivity of GQuEST, and its contributions are shown (orange, blue, gray, gold, lime green, pink, and violet). The standard quantum limit from shot noise $\sqrt{S_L^q}$, which GQuEST is not subject to thanks to its photon counting readout, is also shown (purple dotted line). The contributions of the coating and the substrate to the total mechanical noise S_L^{MN} at local minima are plotted as the curves $\sqrt{S_L^{CMN}}$ (dashed blue), and $\sqrt{S_L^{SMN}}$ (dashed brown), respectively (see Appendices A.4 a and A.4 b). The dark blue vertical dashed line marks the peak signal frequency f_{pk} . The green vertical dashed line marks the fiducial cavity offset frequency ϵ_r ; note that the filter bandwidth $\Delta\epsilon = 25$ kHz is narrower than the thickness of that line in this plot.

a. Elastic Solid Normal Modes in the Optics

Solid normal modes (SNMs) are the resonances of elastic body waves in the optical substrate materials. To analytically model the noise from SNMs in the optics, we start by considering the power spectral density of the displacement noise imparted on the light by a single mechanical resonance peak. We consider a complete set of orthogonal normal mechanical modes (SNMs) identified by their eigenfrequency $\{\omega_\kappa\}$, where κ runs over all modes. These SNMs are obtained by solving the elastic wave equation. The noise PSD from a single SNM is [61]

$$S_L^{MN_\kappa}(\Omega) = C_\kappa \frac{4k_B T}{m\Omega(\omega_\kappa)^2} \left(\frac{Q_\kappa}{1 + Q_\kappa^2((\Omega/\omega_\kappa)^2 - 1)^2} \right), \quad (\text{A.5})$$

where C_κ is a dimensionless parameter that describes the coupling of a mode to the incident light beam. It is related to the analogous mass-scale parameter α_n defined in [61] as $C_\kappa = 1/\alpha_n$, but we use a more convenient convention for summations. The mechanical quality factor, Q_κ , of the mode κ , corresponds to the dissipative loss of the mode and can be decomposed as

$$\frac{1}{Q_\kappa} = \sum_i \frac{U_{\kappa,i}}{U_\kappa^{\max}} \varphi_{\kappa,i}, \quad (\text{A.6})$$

where the sum runs over the different parts or layers of the optic, i.e. the coating layers and the substrate; $\varphi_{\kappa,i}$ and

$U_{\kappa,i}$ are the effective loss angle and elastic energy of the i^{th} part for the mode κ , respectively, and U_κ^{\max} is the total elastic energy in the mode κ . The other parameters in the equation are defined in Table II. We also refer to the contributions of the optical coating and the substrate to the quality factors as Q_c and Q_s , which represent parts of the sum in Eq. (A.6), i.e. the sum over either just the coating or the substrate, respectively. Note that evaluating Eq. (A.6) requires evaluation of the fractional energies stored in the substrate $U_{\kappa,s}$ and the coatings $U_{\kappa,c}$, as well as knowledge of the effective loss angles in each part ($\varphi_{\kappa,s}, \varphi_{\kappa,c}$). While $U_{\kappa,s}, \varphi_{\kappa,s}$, and $\varphi_{\kappa,c}$ can be measured or obtained from solid mechanics theory, the evaluation of $U_{\kappa,c}$ requires a different treatment, as we explain in Appendix A.4 b.

The total displacement noise due to SNMs in the optic is

$$S_L^{MN}(\Omega) = \sum_\kappa S_L^{MN_\kappa}(\Omega). \quad (\text{A.7})$$

To identify all the modes and evaluate this sum, we use a Helmholtz decomposition of the elastic wave equations. This separates the modes into longitudinal (pressure) P-wave and transverse (shear) S-wave terms, which each have a different stiffness given by the P-wave modulus M_s and S-wave modulus G_s , respectively. Note that the P-wave modulus, $M_s = E_s(1 - \nu_s)/(1 - \nu_s - 2\nu_s^2)$, is the stiffness of purely longitudinal (axial) deformation, which is a different quantity than both the Young's modulus, E_s , and the bulk modulus. The shear modulus is $G_s = E_s/2(1 + \nu_s)$. The different elastic moduli of the two wave types lead

to different wave propagation speeds, so these waves resonate at frequencies with different spacings such that the resonances do not overlap at high frequencies. This also means the S- and P-wave resonances do not strongly couple at the boundaries, which allows the P-wave and S-wave modes to be treated independently, simplifying the mode decomposition. The decomposition of the substrate's normal modes has been performed analytically for a square-shaped mirror, and the quadrature sum of noise from both end mirrors and the beamsplitter yields the curve S_L^{MN} as plotted in Fig. 5. We note that high-Q modes expressed by Eq. (A.5) may not be resolved given the finite frequency resolution of Fig. 5, but we integrate the average spectral density over each frequency bin so the plot accurately indicates RMS noise density.

The analysis above predicts that the mechanical noise spectrum will be dominated by regularly spaced peaks corresponding to the mechanical resonances (SNMs) with a wavevector that is mostly parallel to the incident beam. These resonance peaks occur at frequencies $\Omega = n\omega_\kappa = n\pi v_s/h$, $n \in \mathbb{Z}$, where v_s is the phonon propagation speed, and h is the longitudinal dimension of the optic (parallel to the beam, i.e. the thickness). $v_s = \sqrt{M_s/\rho_s}$ for P-waves and $v_s = \sqrt{G_s/\rho_s}$ for S-waves. The lowest-order SNMs have frequencies that are well below the measurement band of the GQuEST experiment. The density of SNM modes in frequency space is expected to grow quadratically with frequency. Therefore, as the modes are thermally populated according to the equipartition theorem, one might expect the total noise to grow at high frequencies. However, the noise is reduced because the coupling to the incident Gaussian beam (parameterized by C_κ) of higher-order modes, i.e. those where the vector that defines the direction of oscillation has a large component perpendicular to the beam axis, scales as

$$C_\kappa \propto e^{-w^2 \mathbf{k}_\perp^2/4}, \quad \mathbf{k}_\perp^2 \equiv \mathbf{k}^2 - (\mathbf{k} \cdot \mathbf{n})^2, \quad (\text{A.8})$$

where \mathbf{k} is the SNM wavevector, \mathbf{n} is the unit vector parallel to the beam axis, and \mathbf{k}_\perp is the transverse wavevector. The S-waves, which are by definition transverse (shear) waves, only produce motion of the reflecting surface when their wavevector has a component perpendicular to the beam axis. Therefore the contributions to the noise of S-wave resonances are reduced (by a factor $\mathcal{O}(10^2)$ in noise power) compared to the P-wave modes. Subsidiary higher-order SNM peaks near a primary SNM resonance add noise on top of the noise floor (see Fig. 5). This contribution can be mitigated by using a large beam radius w , which reduces the coupling of modes with wavevectors perpendicular to the beam.

The strategy for GQuEST is to tune the output filter cavities such that a signal can be measured at frequencies between the P-wave SNM noise peaks, at the noise floor of $\bar{S}_L^c \approx S_L^{\text{MN}}(\Omega)$.

To motivate our choice of optic substrate material and thickness, we consider the level of the resulting noise floor between the mode peaks at the measurement readout frequency ϵ_r due to the properties of the substrate, factoring

out the effect of coatings. We thus decompose the total mechanical noise as

$$S_L^{\text{MN}}(\Omega) \geq \bar{S}_L^{\text{SMN}} + \bar{S}_L^{\text{CMN}}(\Omega), \quad (\text{A.9})$$

where the superscripts indicate the respective contributions to the noise floor from Substrate Mechanical Noise (SMN) and Coating Mechanical Noise (CMN); the latter is later derived in Eq. (A.13). Eq. (A.9) holds as an approximate equality at local minima of $S_L^{\text{MN}}(\Omega)$ at higher frequencies, where the coupling of high transverse-wavenumber modes (i.e. modes for which $w^2 \mathbf{k}_\perp^2 \gg 1$) is greatly reduced (see Eq. (A.8)). We express the contribution to the noise floor from mechanical dissipation in the substrates (parameterized by $Q_s = 1/\varphi_s$) using the following approximate analytical expression:

$$\bar{S}_L^{\text{SMN}}(\Omega) \approx \frac{16k_B T h}{\pi^3 v_s^2 \rho_s w^2 Q_s \Omega} = \frac{16k_B T h \varphi_s}{\pi^3 M_s w^2 \Omega}. \quad (\text{A.10})$$

This equation defines a curve that intersects the local minima of the SNM noise when the effect of coatings is neglected. We leave the derivation of this expression for future work, but provide it to indicate the scaling of the noise floor with design parameters. To increase the frequency separation between mechanical resonances and lower the noise floor between them, a thinner and stiffer optic with a higher quality factor is desirable. The mechanical quality factor of the silicon substrate is expected to be limited by Akhiezer damping and is given by $Q_s \cdot \Omega = 3 \cdot 10^{15}$ Hz [62] for Q_s as given in Table II evaluated at $\Omega = 2\pi\epsilon_r$. This frequency dependence of the quality factor makes the PSD (Eq. (A.10)) flat, as seen in Fig. 5. The fiducial design uses crystalline silicon optics with a thickness of $h = 2$ mm.

In addition to the computation of the noise from SNMs via the decomposition of the optic's excitation into normal modes, i.e. the evaluation of Eq. (A.7), the expected thermal noise spectrum from SNMs has also been modeled with Levin's direct method. This was done numerically using COMSOL Multiphysics[®], a finite element modeling program that performs the necessary volume integrals over energy and dissipation. Both modeling methods agree on the level of the noise floor $S_L^{\text{MN}}(\epsilon_r) \approx (10^{-21} \text{ m}/\sqrt{\text{Hz}})^2 \approx S_L^c(\epsilon_r)$. Moreover, the analytical model agrees with data from the Fermilab Holometer [19]. The model captures the characteristic "sawtooth" shape in the measured noise spectrum that arises from the density of SNM states and the coupling to the Gaussian beam mode.

Mechanical thermal noise also arises from the mirrors that compose the power-recycling cavity. This noise does not typically impact homodyne readout, as the noise is common between the arms and therefore only appears in the amplitude quadrature of the optical field at the output, whereas the signal is in the phase quadrature. However, photon counting measures signal and noise in both optical quadratures and is thus in principle sensitive to common-mode noise, if this noise is coupled to the output through asymmetries intrinsic to the interferometer.

However, common-mode thermal noise, like input laser noise, is suppressed by the power-recycling cavity and attenuated by operating the interferometer close to a dark fringe, making it subdominant to thermal noise in the end mirrors and beamsplitter.

Finally, SNMs of the optics also scatter light from the fundamental optical mode into higher-order modes. We anticipate that this scattering into higher-order modes will not be negligible and will change the frequency dependence of the noise spectral density from higher-order SNMs. We expect that the readout filter cavities will fully suppress this effect as they reject higher-order optical modes, but leave analysis of this effect for future work.

b. Mechanical Thermal Noise from Optical Coatings

Equation (A.7) and the corresponding curve in Fig. 5 fully incorporate the thermal noise from the optics, including the contribution added by optical coatings through Eq. (A.6) in the form of $Q_c = 1/\varphi_c$. We evaluate this contribution separately in this section as it requires a different approach to the evaluation of the contribution of the substrate Q_s . We find the loss in the coatings contributes significantly to the noise floor, as represented by Eq. (A.9), and we refer to this contribution as the coating mechanical noise (CMN).

The multi-layer Bragg-reflector coatings exhibit both mechanical (homogeneous) dissipation and thermal diffusion (inhomogeneous dissipation). Both forms of dissipation contribute noise to the optical beam. The homogeneous term relating to mechanical noise is considered here, while the latter term from thermal diffusion is called thermo-optic noise and treated in Appendix A.5 b.

Beyond the mechanical vibrations of the reflecting (front) surface of the optic, additional mechanical effects influence the light. Mechanical excitations inside the coating entail changes of the size and index of refraction of the layers of the Bragg-reflector coating, which in turn gives rise to fluctuations of the reflection phase of the incident optical field [40]. We do not consider the effect of reflection phase changes here, as it is a subdominant $\mathcal{O}(30\%)$ contribution in GW detectors [40, 58].

The mechanical noise of the coating can be treated in unison with that of the substrate, by applying solid mechanics theory for a composite solid [63]. However, solving the homogeneous elastic wave equations for the compound optic does not provide the correct value for $U_{\kappa,c}$, as the free boundary conditions imply no energy is stored in the coatings when a normal mode is excited and no significant noise is contributed by the coatings, which is contrary to experimental observation and alternative theoretical treatments.

To estimate the coating mechanical noise, the elastic wave equation must be solved with a force at the boundary that corresponds to the incident beam, whereby we utilize Levin's direct method while treating an optic of finite size. The solution of the wave equation provides the

admittance Y_κ of the optic surface when acted on by the force at the boundary, which now contains the total Q_κ according to Eq. (A.4). The energy stored in the coatings $U_{\kappa,c}$ can then be obtained by factorization of Eq. (A.6), which finally allows the total mechanical noise to be computed in Eq. (A.7).

This factorization uses measured values of the mechanical loss angles of the coatings $\varphi_{\kappa,c}$. The mechanical loss angles of the high-reflection optical coatings used in aLIGO mirrors have been inferred from direct measurements of the CMN at frequencies from 30 Hz to 2 kHz in [64]. These coatings are made of alternating layers of SiO_2 and either Ta_2O_5 or $\text{TiO}_2 : \text{Ta}_2\text{O}_5$. For Ta_2O_5 the measurements give

$$\varphi_{\text{Ta}} = (5.3 \pm 0.1) \cdot 10^{-4} \left(\frac{f}{100 \text{ Hz}} \right)^{0.06 \pm 0.02}. \quad (\text{A.11})$$

To estimate $\overline{S}_L^{\text{CMN}}$ in the GQuEST experiment, we assume a coating design similar to aLIGO (i.e. the same number and thickness of alternating layers of SiO_2 and Ta_2O_5) with φ_{Ta} as given by Eq. (A.11) and $\varphi_{\text{SiO}_2} = 5 \cdot 10^{-5}$. We then extrapolate from the measurements in [64] and assume these values are accurate at frequencies in the band $\approx 1\text{-}40$ MHz. Specifically, we use

$$\varphi_{\kappa,c} = \sum_{i=1}^{N_{\text{coat}}} \varphi_{c,i} \frac{2h_{c,i}M_{c,i}}{h_c M_s} \quad \text{where } \varphi_{c,i} = \begin{cases} \varphi_{\text{Ta}} & i \text{ even} \\ \varphi_{\text{SiO}_2} & i \text{ odd,} \end{cases} \quad (\text{A.12})$$

where $h_{c,i}$ are the thicknesses of each coating layer, $h_c = \sum h_{c,i}$ is the total coating thickness, $\varphi_{c,i}$ are the loss angles of each layer, and $M_{c,i}$ is the P-wave modulus of the i^{th} coating layer. When considering S-waves, i.e. for certain κ , $M_{s,c}$ should be replaced with $G_{s,c}$ in this equation. These moduli can be calculated from the coating's Young's modulus and Poisson ratio using the same formula as for the substrate's moduli.

By considering $\varphi_c \approx \varphi_{\kappa,c}$, and including only the dominant P-wave contributions in the computation of $\varphi_{\kappa,c}$, we now evaluate the contribution of the coatings to the SNM thermal noise floor at the measurement frequency. When only including contributions from the coating to the total loss angle, we find the following analytical expression for the solid normal mode thermal noise floor:

$$\overline{S}_L^{\text{CMN}}(\Omega) \approx \frac{16k_B T h_c \varphi_c}{\pi^3 M_s w^2 \Omega}, \quad (\text{A.13})$$

The remaining parameters are defined in Table II. This equation is analogous to Eq. (A.10), except it uses the thickness and loss of the coating rather than those of the substrate. Together, Eqs. (A.10) and (A.13) can be used to evaluate Eq. (A.6), to give an effective description of the two dominant dissipation contributions as $1/Q_\kappa \approx \varphi_s + (h_c/h)\varphi_c$. Note however that the substrate modulus M_s appears in the denominator of both Eqs. (A.10) and (A.13) and in Eq. (A.12) due to its dominant contribution to all SNM mode energies. The form of Eq. (A.13) is comparable to the form of Eq. 1 of [58], though it has different weighting factors of the elastic moduli.

In conclusion, we find thus that the effective contributions to the total quality factor of the coating $Q_c \approx 1400$, compared to that of the substrate $Q_s \approx 10^6$, while the coating is roughly 200 times thinner than the substrate. Despite this, the coating contributes 3-4 times as much noise as the substrate.

A.5. Thermorefractive and Thermoelastic Noise in the Optics

Thermorefractive noise and thermoelastic noise, collectively called thermo-optic noise, are due to random fluctuations in temperature in the optics from inhomogeneous dissipation. These temperature fluctuations produce corresponding changes in the index of refraction and the size of optical substrates and coatings. The changes are proportional to the materials' thermorefractive coefficients and coefficients of thermal expansion, respectively, and this produces phase noise in the incident beam.

a. Thermo-Optic Noise in Optical Substrates

The main contribution of thermo-optic noise in the optical substrates to the total noise in the IFO output is thermorefractive fluctuations in the beamsplitter. The power spectral density of substrate thermorefractive (STR) noise is given by the following equation [65, 66]:

$$S_L^{\text{STR}}(\Omega) = \frac{4k_B\kappa_s T^2 \beta_s^2 h}{\pi(C_s \rho_s w^2 \Omega)^2}. \quad (\text{A.14})$$

For the fiducial design parameters of the GQuEST experiment, the thermorefractive noise amplitude spectral density (ASD) at the measurement frequency $\Omega/2\pi = \epsilon_r \approx 17.6$ MHz is thus $\sqrt{S_L^{\text{STR}}} = \mathcal{O}(10^{-22})$ m/ $\sqrt{\text{Hz}}$. However, the measured noise at the interferometer output is modulated by the transfer function for phase modulations imparted at the beamsplitter $H(\Omega) = \cos^2(\Omega L/c) \leq 1$. Thus, the total thermorefractive noise measured is $H(\Omega)S_L^{\text{STR}}(\Omega)$.

Thermoelastic noise arises from random fluctuations in temperature that result in thermal expansion of all the optics (not just the beamsplitter). The power spectral density of substrate thermoelastic (STE) noise in our measurement band is [67],

$$S_L^{\text{STE}}(\Omega) = \frac{8}{\sqrt{2\pi}} \frac{k_B\kappa_s T^2 \alpha_s^2 (1 + \nu_s)^2}{C_s^2 \rho_s^2 w^3 \Omega^2}, \quad (\text{A.15})$$

where the variables are defined in Table II. For the reference design, the thermoelastic noise ASD at 17.6 MHz is $\sqrt{S_L^{\text{STE}}} = \mathcal{O}(10^{-23})$ m/ $\sqrt{\text{Hz}}$. While the thermorefractive and thermoelastic noise in silicon is larger than in conventional fused silica optics, these noises are both well below the noise floor from solid normal modes. The thermoelastic noise from the beamsplitter (but not that from the end mirrors) will be modulated by $H(\Omega)$.

b. Thermo-Optic Noise in Optical Coatings

In this section, we consider the effects of thermoelastic and thermorefractive fluctuations in the optical coatings (CTE and CTR noise, respectively); we refer to their combined effect as coating thermo-optic (CTO) noise: $S_L^{\text{CTO}} = S_L^{\text{CTE}} + S_L^{\text{CTR}}$. The CTO noise $S_L^{\text{CTO}}(\Omega)$ is plotted in Fig. 5. We use the model in [68] as a starting point and follow their notation. However, their model describes noise at relatively low frequencies, as relevant in gravitational-wave detectors. Several key physical assumptions must therefore be reconsidered to model noise in the GQuEST measurement band. In particular, the coherence properties of this noise and its frequency dependence are different at higher frequencies, and this must be accounted for. Specifically, at low frequencies, the CTO and CTR contributions coherently cancel each other, while at high frequencies the noises are independent. In addition, at high frequencies, thermal fluctuations have coherence lengths that are shorter than the relevant physical coupling scale, which means the effect of the thermal fluctuations averages out to some degree, as explained below.

The PSDs of CTE and CTR noise are [68–70]

$$S_L^{\text{CTE}}(\Omega) = \frac{2\sqrt{2}k_B T^2 \Gamma_{\bar{\alpha}}(\Omega)}{\pi w^2 \sqrt{\kappa_c \rho_c C_c \Omega}} \left(\bar{\alpha}_c h_c - \bar{\alpha}_s h_c \frac{C_c}{C_s} \right)^2, \quad (\text{A.16})$$

$$S_L^{\text{CTR}}(\Omega) = \frac{2\sqrt{2}k_B T^2 \Gamma_{\bar{\beta}}(\Omega)}{\pi w^2 \sqrt{\kappa_c \rho_c C_c \Omega}} (\bar{\beta}_c \lambda)^2, \quad (\text{A.17})$$

where the overbars denote averaged effective coating material properties as defined in [68], and we introduce the dimensionless cut-off parameters $\Gamma_{\bar{\alpha}}(\Omega)$ and $\Gamma_{\bar{\beta}}(\Omega)$; the other variables are defined in Table II. These cut-off parameters parameterize the effect that thermal fluctuations with a scale smaller than the size of the part of the material that couples the fluctuations to the incident light are averaged out, and thus their effect diminishes. The scale of the thermal fluctuations is given by the thermal diffusion length $r_T \equiv \sqrt{\kappa_c / \rho_c C_c \Omega} \approx 0.1$ μm for $\Omega = 2\pi \cdot 17.6$ MHz (see [68]). The scale of the thermoelastic coupling is the thickness of the coating h_c , as fluctuations throughout all layers contribute to the overall shift of the reflecting surface. The scale of the thermorefractive coupling is the depth that the optical field penetrates into the coating, $\bar{\lambda}$, given below. In the fiducial design $r_T < \bar{\lambda} \ll h_c$, which effects an additional roll-off rate of $1/\Omega$ in the CTE and CTR PSDs in the measurement band and therefore greatly reduces these noises.

The asymptotic forms (i.e. at low and high frequencies) of the cut-off parameters for the CTE and CTR contributions, respectively, are

$$\Gamma_{\bar{\alpha}}(\Omega) = \frac{1}{\mathcal{O}(1 + R(1 + R)h_c^2/r_T^2)}, \quad \Gamma_{\bar{\beta}}(\Omega) = \frac{1}{\mathcal{O}(1 + 2\bar{\lambda}^2/r_T^2)}, \quad (\text{A.18})$$

where $R = \sqrt{\kappa_c \rho_c C_c / \kappa_s \rho_s C_s}$, $\bar{\lambda}$ is defined below, and the other variables are defined above. The exact expression

for $\Gamma_{\bar{\alpha}}$ is given in [68] where it is referred to as the thick coating correction, and is considered in more physical detail in section IV.C.3 of [71]. This cut-off parameter causes coating thermo-optic noise to be dominated by the thermorefractive term.

The parameter $\Gamma_{\bar{\beta}}$ has not been considered in previous work; it gives the cut-off of the CTR, and is a function of the depth that the optical field penetrates into the coating $\bar{\lambda}$. Specifically, we have that the intensity I decays exponentially as a function of the distance traveled into the coating z with the decay constant $\bar{\lambda}$:

$$I(z > 0) \propto e^{-z/\bar{\lambda}} \quad \bar{\lambda} = \frac{\lambda}{8 \ln(n_H/n_L)} \left(\frac{1}{n_L} + \frac{1}{n_H} \right) \quad (\text{A.19})$$

where n_H and n_L are the indices of refraction of the high and low index of refraction coating layers, respectively. Previous work uses the approximation that the beam does not penetrate beyond the surface of the coating (cf. the delta function of Eq. 32 in [68]), which is valid as those works model noise in the regime $r_T \gg \bar{\lambda}$. For the fiducial GQuEST design, $\bar{\lambda} \approx 0.62 \mu\text{m}$.

For the CTE and CTR noise PSDs plotted in Fig. 5, we use the exact form for $\Gamma_{\bar{\alpha}}$ from [68] and the approximate form for $\Gamma_{\bar{\beta}}$ given above, which we expect is accurate within a factor of 2.

The cut-off scales are important in modeling CTO noise, as they render what would otherwise be the dominant noise source at the measurement frequency subdominant. Future work will establish an exact form for $\Gamma_{\bar{\beta}}$, and should use a more precise description of the optical field in the coating, capturing the fact that the incident field is a standing wave that experiences discretized attenuation through successive layers. This description may add additional frequency scales corresponding to the thicknesses of individual layers ($\lambda/4$ or $\lambda/2$).

A.6. Charge Carrier Noise in the Beamsplitter

For semi-conducting optics, another source of thermal noise inherent to the substrate needs to be considered. Thermal density fluctuations of the electrons in the conduction band of the material produce local fluctuations in the refractive index, which produces a noise with a PSD

$$S_L^{\text{SCC}}(\Omega) = \frac{8Dk^2 \alpha_e^2 N_0 h}{\pi w^2} \left[\frac{1}{\Omega^2 + (4Dk^2 + D/l_D^2)^2} \right]. \quad (\text{A.20})$$

Here, $\alpha_e = \partial n / \partial N$ where N is the local number density of charge carriers (see [72], where α_e is called α), N_0 is the mean number density of charge carriers for the material, which is calculated in [73], where N_0 is called n_0 . The other variables are defined in Table II.

For a silicon beam splitter at 294 K, as in the fiducial design, we expect the charge carrier noise to be $\sqrt{S_L^{\text{SCC}}} \leq \mathcal{O}(10^{-22}) \text{ m}/\sqrt{\text{Hz}}$ based on the analysis in [72]. Similar to thermorefractive noise, this noise source is also

modulated by the transfer function of phase modulations imparted at the beamsplitter $H(\Omega)$. Practically, this calculation indicates that beamsplitter substrates should have a high resistivity and correspondingly a low dopant concentration, in which case this noise contribution will be negligible.

A.7. Thermal Lensing in the Beamsplitter

As the incident laser beam is partially absorbed by the coating and substrate of the beamsplitter, and because the beam has a non-constant cross-sectional intensity profile, a thermal gradient is formed transverse to the optic axis. Due to the nonzero thermo-optic coefficient $\beta = \partial n / \partial T$, the transmitted light is lensed. This ‘thermal lens’ effectively converts the incident fundamental-mode light into higher-order modes. As only the light transmitted through the beamsplitter is lensed, the effect is differential and thus increases the contrast defect of the interferometer. Silicon has a higher thermal conductivity than fused silica, and therefore the thermal gradient and the resulting thermal lensing are reduced compared to high-power interferometers using a fused silica beamsplitter.

The fraction of the contrast defect power output from the Michelson can be computed using the Laguerre-mode overlap integrals in [74] and accounting for the number of beam passes. This simplifies to the expression:

$$\Lambda_{\text{defect}} = 0.07 \eta \left(\frac{\beta}{\kappa \lambda} (\Lambda_c + \Lambda_s) P_{\text{BS}} \right)^2, \quad (\text{A.21})$$

where Λ_{defect} is the fractional power loss into higher-order modes from the wavefront distortion. Λ_s , the power absorbed in the substrate, is equal to the thickness of the substrate times the absorption per unit length. The coefficient 0.07 is a geometrical factor that represents the sum of the squared inner products of all higher-order modes with the transverse profile of the thermal lens. The inner products are calculated using Eq. 7 of [74]. The other variables are defined in Table II.

The factor $\eta \approx 0.94 \cos^2(2\phi_g) + 0.06$ incorporates the one-way Gouy phase advance ϕ_g of the beam going down an interferometer arm, assuming a beam waist either at the beamsplitter or at the end mirror. We indicate the effect of η to show that thermal lensing can be reduced in interferometers with specific Gouy phase to cancel the contribution from the first-order Laguerre-Gauss modes to contrast defect light. GQuEST will use beams with large radii w to suppress mechanical noises (see above), which entails that $\phi_g \ll 45^\circ$ and $\eta \sim 1$.

The contrast defect power due to thermal lensing is then

$$P_{\text{ASdefect}} = \Lambda_{\text{defect}} P_{\text{BS}}. \quad (\text{A.22})$$

For GQuEST’s design, $\Lambda_{\text{defect}} = 2 \text{ ppm}$ and therefore we estimate that $P_{\text{ASdefect}} = 20 \text{ mW}$. The effect of thermal lensing is proportional to the square of the substrate material property β_M / κ_M . For fused

silica, $(\beta_{\text{FS}}/\kappa_{\text{FS}})^2 = 3.6 \cdot 10^{-11} (\text{m/W})^2$, while for silicon, $(\beta_{\text{s}}/\kappa_{\text{s}})^2 = 1 \cdot 10^{-14} (\text{m/W})^2$; the choice of silicon therefore produces a reduction of thermal-lensing-induced contrast defect power by a factor $\mathcal{O}(10^3)$.

For reference, using the same model to compute the expected thermal lensing for the case of the Fermilab Holometer [19], we find a value that agrees with the measured power lensed to within an order of magnitude. Therefore, the estimate for the thermal lensing in the GQuEST experiment is expected to be similarly accurate.

A.8. Optic Curvature due to Coating Stress

High-reflectivity (HR) mirrors comprise dielectric (Bragg) reflection coatings applied to an optical substrate. This coating introduces elastic stress to the mirror surface, which changes the mirrors' radius of curvature. The effects of coating stress are expected to be greater for GQuEST than in other precision interferometers, as we use relatively thin optics to increase the frequency separation of mechanical resonances, and the coating stress therefore introduces more curvature than would occur for a thicker and thus stiffer mirror. The curvature induced in a flat mirror due to coating stress can be approximated in terms of its radius of curvature r_{curv} and optical power $D = 2/r_{\text{curv}}$ using the Stoney equation [75], which gives

$$r_{\text{curv}} \approx \frac{1}{6} \left(\frac{E_s h^2}{\sigma_c h_c (1 - \nu_s)} \right), \quad D \approx 12 \left(\frac{\sigma_c h_c (1 - \nu_s)}{E_s h^2} \right), \quad (\text{A.23})$$

where the variables are defined in Table II. Note that this approximation is valid for $\frac{h_c}{h} \ll 1$; for the GQuEST mirrors $\frac{h_c}{h} = \mathcal{O}(10^{-2})$. Using the proposed experimental parameters, this gives an induced curvature of $r_{\text{curv}} = 7.6 \text{ m}$ or 0.26 diopters of spurious focusing power.

Differences in the induced curvature between the end mirrors would lead to a 'mode mismatch' between the arms of the interferometer, which produces a contrast defect consisting of HOMs. Specifically, a difference in the stress-induced curvature of the end mirrors along a direction x, y orthogonal to the beam axis, i.e. $D_x = D_x^{\text{EMX}} - D_x^{\text{EMY}}$ scatters light from the fundamental mode into the (Hermite-Gauss) HG20 and HG02 modes with amplitude coefficients [76]

$$K_{20} \approx \frac{1}{\sqrt{2}} \left(\frac{k D_x w^2}{4} \right), \quad \text{and} \quad K_{02} \approx \frac{1}{\sqrt{2}} \left(\frac{k D_y w^2}{4} \right) \quad (\text{A.24})$$

where the parameters are in Table II. This scattering then gives rise to a contrast defect $\Lambda_{\text{CD}} = K_{02}^2 + K_{20}^2$. Thus, to achieve $\Lambda_{\text{CD}} < 10 \text{ ppm}$, we require that the curvature mismatch between end mirrors $D_{\text{tot}} = \sqrt{D_x^2 + D_y^2} < 3 \cdot 10^{-4} \text{ diopters}$. This indicates that the coating-stress-induced curvature calculated above must somehow be compensated to satisfy this condition. We intend to partially compensate for the curvature induced by the HR coating by applying an AR coating with

a custom thickness to the back of the optic, such that the stress induced by the AR coating cancels the curvature induced by the HR coating. However, this method requires a priori knowledge of the induced coating stress, and as modeling of this coating stress will likely only be accurate to within $\approx 1 - 10\%$, the curvature can only be compensated to that fraction. The remaining residual differential curvature will be compensated using custom mirror mounts that actuate on the mirror such that its curvature can be corrected by an amount $\mathcal{O}(10) \text{ mD}$ along two independent axes.

A.9. Optical Cavities to form the Narrow Band-Pass Readout Filter

The circulating power incident on the beamsplitter of $P_{\text{BS}} = \mathcal{O}(10) \text{ kW}$ corresponds to $\mathcal{O}(10^{23})$ photons/s. A contrast defect $\Lambda_{\text{CD}} = \mathcal{O}(10) \text{ ppm}$ would amount to $P_{\text{out}} = \mathcal{O}(0.1 \text{ W} \approx 10^{18})$ photons/s at the interferometer output. Our goal is to suppress this light to achieve a photon flux smaller than that from the interferometer thermal noise ($\mathcal{O}(10^{-2}) \text{ Hz}$) at the signal peak frequency. Therefore, in total, $\mathcal{O}(200) \text{ dB}$ of power suppression of carrier laser light is needed. GQuEST's design includes four filtering cavities, each providing nearly 60 dB of suppression, to meet this goal.

These filter cavities have a bow-tie geometry, with an optical path length of approximately 2.4 m, giving a free spectral range (FSR) of roughly 125 MHz (see Fig. 6). The input and output couplers (mirrors) are given transmissivities of $T_I = T_O = 1000 \text{ ppm}$, and therefore the finesse of each cavity is $\mathcal{F} \approx \pi/T_I = 3150$ and their bandwidth is $\Delta\epsilon_1 = 42 \text{ kHz}$. Within the resonant bandwidth of each cavity, approximately 98% of the light is passed and 2% is lost, assuming 10 ppm of optical loss on each optic. Moreover, the filter cavity lengths will all be slightly different to give them slightly different FSRs, which prevents light at frequencies that are a multiple of the FSR from leaking through the filter cavities.

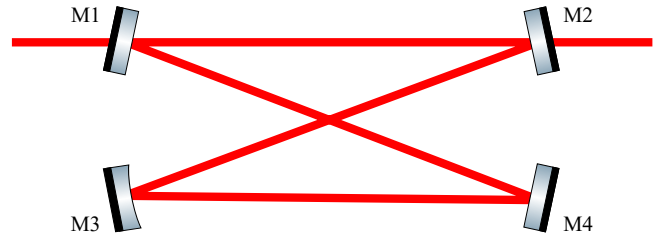


FIG. 6. The optical layout of the optical bow-tie filter readout cavities, comprised of four mirrors M1-M4. Note that M3 is curved for cavity stability and design of the round-trip Gouy-phase.

The filter function for a single output filter cavity is Lorentzian, and therefore the power attenuation of four cavities follows

$$F(\epsilon - \epsilon_r) = \left(\frac{\Delta\epsilon_1^2}{\Delta\epsilon_1^2 + 4(\epsilon - \epsilon_r)^2} \right)^4. \quad (\text{A.25})$$

Here, $\Delta\epsilon_1$ is the bandwidth of a single cavity. The integrated bandwidth $\Delta\epsilon = \int_{-\infty}^{\infty} F(\epsilon) d\epsilon \approx \Delta\epsilon_1/2$. Based on this filter shape, ϵ_r cannot be set arbitrarily low while maintaining sufficient filter performance, as the suppression of carrier light at a frequency ν (corresponding to $\epsilon = 0$) is reduced for $\epsilon_r \rightarrow 0$. Specifically, below an offset frequency of $\epsilon_r^{\min} \approx 8$ MHz, the filters no longer have sufficiently rapid roll-off to suppress carrier photons, giving a rate of carrier photons reaching the photodetector greater than the flux from classical noise ($\dot{N}_{\text{pass}}^c \approx 1.6 \cdot 10^{-2}$ Hz, Eq. (15)). Likewise, ϵ_r cannot be chosen arbitrarily high, as too much light in higher-order spatial modes is expected to be passed by the cavities at higher frequencies ϵ . The filter cavities are designed to have a round-trip Gouy phase accumulation slightly offset from $2\pi/3$, in either direction. Thus, if the offset frequency from the carrier, ϵ_r , is more than 1/3 of the FSR of the cavity, carrier light in higher-order spatial modes will leak through. This sets $\epsilon_r^{\max} = \text{FSR}/3 \approx 40$ MHz.

A.10. Reduction of SNSPD Dark Counts and Blackbody Background

The main challenge in the implementation of SNSPDs is the reduction of dark counts, i.e. signals in the absence of any light. The origin of intrinsic dark counts in SNSPDs is an ongoing topic of research but is expected to be thermally activated single-vortex crossing events [77, 78], the rate of which has an exponential dependence on the bias current [79, 80]. The intrinsic detection efficiency, however, saturates at a certain threshold bias current, it is thus advantageous to bias the detector at this point, where the dark count rate can be $< 10^{-5}$ Hz [34]. To reach sufficiently low intrinsic dark count rates, the SNSPD will be operated at a temperature < 1 K.

Care must also be taken in readout and bias electronics, which can increase the dark count rate in SNSPDs above the intrinsic levels. The use of cryogenic (4 K) amplifiers and bias-tees can significantly reduce electronic noise coupling to the detector, as well as the use of a fully differential readout architecture [81], which minimizes electromagnetic interference and prevents ground-loops in the circuitry.

It is important to ensure minimal coupling of background light to the photon detector as well as rejection of any black-body radiation since SNSPDs optimized for 1550 nm can be sensitive to photon wavelengths $> 3.0 \mu\text{m}$. By using a single-mode optical fiber between the final, cryogenic, filter cavity and the SNSPD, the background light will be minimized. Ideally, the final filter cavity could also be located in a contiguous cryogenic radiation shield with the detector.

If additional short-pass and narrow-band filtering of the signal is deemed necessary, an effective approach could be

implemented that has recently been demonstrated using custom free-space filters [38]. In this approach, light from the optical fiber would be collimated with a cryogenic lens, and sent through a series of filters, prior to going to being focused onto the SNSPD with another cryogenic lens.

A.11. Coherent Signal Detection Challenges

The scheme for coherent signal detection with two co-located interferometers, using photon counting, shown in Fig. 4 is novel and will therefore entail challenges not encountered in previous experiments. The scheme combines outputs from the two interferometers on a beamsplitter (BS-C) and provides two new output channels: a ‘null’ channel that only contains incoherent noise and a ‘signal’ channel that contains coherent signals and the incoherent noise. The photon flux measured in the null channel can thus be subtracted from the flux measured in the signal channel to estimate the coherent signal power. By changing the relative phase between the two inputs of BS-C ($\Delta\Phi$ as depicted in Fig. 4) the signal and null channels can be switched between the physical output ports of the beamsplitter, which allows the same readout cavities and detector system to be used to measure both channels (at different times) with minimal changes to the system. This helps to reduce possible biases in the measurement of the coherent signal power.

A potential challenge in this scheme is the presence of correlated noise that might be inadvertently introduced by combining the IFO output fields and phase-locking the respective input lasers. If the outputs of the IFOs contain correlated noise sideband fields at the signal frequency, these fields would coherently interfere at BS-C, either constructively or destructively, and would therefore lead to an over- or underestimate of the coherent signal power, respectively. In other words, correlated noise effectively manifests as a spurious positive or negative signal power in the coherent signal detection scheme. This may undermine the coherent detection technique unless this correlated noise can be sufficiently mitigated or quantified precisely. We argue below that this is feasible for several potential sources of correlated noise (CN).

Input laser noise of the two interferometers is a potential source of CN. To ensure that the signal of interest (which is expected to be coherent across the two interferometers) creates coherent sideband signals, the carrier fields in the two interferometers need to be coherent as well. This necessitates phase-locking the two input lasers together, which will be performed using a feedback control loop with a bandwidth of roughly 100 kHz. This has the drawback that noise introduced by this phase-lock feedback control system (controls noise) used to lock both lasers would be coherent between the instruments to a significant degree. However, since the control system will be operating at frequencies well below the nominal filter offset frequency ϵ_r , the magnitude of correlated laser noise introduced thus is greatly reduced above the controller’s

bandwidth. In addition, the laser filter cavities and interferometer power recycling cavities will further suppress this noise.

Another potentially significant source of CN is output light at the carrier frequency ($\epsilon = 0$) which is deliberately made coherent between the two IFOs as explained above. This light is suppressed by $\mathcal{O}(240 \text{ dB})$ through the filter cavities (see Section 4.b), but any remaining light manifests as noise. This CN will be characterized by modulating the output light level through changing the relative phase $\Delta\Phi$ between the two outputs of the IFOs, as well as by changing the output light level of either IFO. This testing process will modulate spurious photon flux from the leakage of carrier light while not modulating flux from high-frequency thermal noise processes, which allows this CN source to be appropriately subtracted from the measured coherent signal power in the data. Of related concern is CN from carrier light leaking through the filter cavities in higher-order modes (HOMs). This can be characterized by introducing an aperture into the output beam of a single interferometer to scatter a significant amount of light into HOMs, which then allows the leakage of HOMs through the filter cavities to be characterized. If the filter cavities achieve their fiducial design, the power of carrier light leaking through the filter cavities is expected to be substantially smaller than that of thermal noise at the signal frequency. Therefore, even though leaked carrier light would manifest as CN, it would not produce a significant systematic error in the estimation of the coherent signal power.

Finally, another source of CN is noise imparted by the beamsplitter BS-C or any processes downstream of the combination of the outputs of the two IFOs. However, the power of noise sidebands produced there is proportional to the power of the incident light, and therefore the noise power produced at BS-C will be a factor $P_{\text{out}}/P_{\text{BS}} = \mathcal{O}(10^{-5})$ lower compared to the noise produced at BS-A and BS-B. Because of this known scaling, many potential sources of CN in this part of the experiment can be characterized when operating a single interferometer.

A.12. Additional Subdominant Noise Sources

In addition to those considered above, we have considered the following noise sources: (environmental) seismic noise, noise from residual gas in the interferometer vacuum system, and quantum radiation pressure noise. While these are limiting noise sources for lower frequency interferometers, the PSDs of many of these noises decrease with frequency and are thus very subdominant to mechanical thermal noise at 17.6 MHz. Radiation pressure noise can be significant at high frequencies, as it is proportional to the mechanical susceptibility of the mirrors, and this susceptibility has peaks at the frequencies of the longitudinal solid normal mode resonances. However, quantum radiation pressure is weaker than thermal mechanical noise in the optics (see Appendix A.4 a) in our measurement band.

Another potentially relevant noise is due to air diffusion in the readout part of GQuEST (RAD), i.e. gas noise in the output beams of the interferometers that enters the filter cavities. The coupling mechanism of this noise is similar to that of the residual gas noise in the interferometer vacuum system. However, the important differences are that the air in the readout is at atmospheric pressure and therefore the motion of air molecules is diffusive and the number density is drastically higher. Using the two-point correlator of molecule positions and the Green's function for the Fokker-Planck diffusion equation (Fick's second law), we derive the spectral density. We elide the derivation for conciseness, will include it in future work, and note that this expression agrees with prior numerical results [82]. We find the following noise PSD in the high-frequency limit:

$$S_L^{\text{RAD}}(\Omega) = \frac{4\pi\rho_{\text{air}}L_{\text{air}}D_{\text{air}}}{\Omega^2} \left(\frac{ka_{\text{air}}}{\pi\epsilon_0w_{\text{air}}^2} \right)^2 \frac{P_{\text{out}}}{h\nu G}, \quad (\text{A.26})$$

where the the number density of air $\rho_{\text{air}} = 2.7 \cdot 10^{25} \text{ m}^{-3}$, the mass diffusivity $D_{\text{air}} = 2 \cdot 10^{-5} \text{ m}^2/\text{s}$, the beam radius $w_{\text{air}} \approx 500 \mu\text{m}$, and $a_{\text{air}}/4\pi\epsilon_0 = (n_{\text{air}}^2 - 1)/4\pi\rho_{\text{air}} \approx 2 \cdot 10^{-30} \text{ m}^3$ is the polarizability of air at the laser wavelength λ according to the Lorentz-Lorenz relation. $L_{\text{air}} \approx 4 \text{ m}$ is the approximate path length of the output light through the air between an IFO beamsplitter (BS-A/BS-B) and the output of the first readout filter cavity. The path length inside the first readout cavity is included, as it resonantly enhances air noise sidebands at the readout frequency as much as it attenuates the carrier light. In effect, extra air diffusion noise is produced equivalent to the noise produced by light propagating for the length of the cavity. After the first cavity, the carrier light is suppressed significantly, and noise imparted in the other cavities is negligible. While the noise scales with w_{air}^{-4} , the air diffusion noise S_L^{RAD} is subdominant as shown in Fig. 5. Readout air diffusion noise downstream of BS-C will manifest as correlated noise, but it is not fundamental and can be removed by reducing the path length in the air or putting the first readout cavity in a vacuum chamber.